Abdel Azim *et al. Geothermal Energy* (2024) 12:26
https://doi.org/10.1186/s40517-024-00305-6

Geothermal Energy

RESEARCH **Open Access**

A fully coupled thermo-poroelastic model for energy extraction in naturally fractured geothermal reservoirs: sensitivity analysis and flow simulation

Reda Abdel Azim[1*], Saad Alatefi[2] and Abdulrahman Aljehani[3]

*Correspondence:
reda.abdulrasoul@auk.edu.krd

[1] Petroleum Engineering Department, American University of Kurdistan, Kurdistan Region of Iraq, Duhok, Iraq
[2] Department of Petroleum Engineering Technology, College of Technological Studies, PAAET, 70654 Kuwait City, Kuwait
[3] Faculty of Earth Sciences, King Abdulaziz University, 21589 Jeddah, Saudi Arabia

Abstract

The development of a novel method for modelling fluid flow and heat transfer in naturally fractured geothermal reservoirs represents a significant advancement in geothermal energy research. This Study presents a hybrid approach, which combines discrete fracture and single continuum techniques, to effectively capture the complex interactions between fluid flow and heat transfer in geothermal fractured reservoirs. In addition, the incorporation of the local thermal nonequilibrium method for simulating heat transmission accounts for the disparities in temperature between the rock matrix and the fluid, providing a more realistic representation of heat transfer processes. The study also presents a fully coupled thermo-poro-elastic framework that integrates fluid flow and heat transfer to comprehensively evaluate reservoir responses to injection/production scenarios. This coupled approach allows for the prediction of changes in reservoir properties, such as permeability and porosity, under varying fluid pressure and temperature conditions. The application of the proposed model to evaluate a geothermal reservoir's long-term response to injection/production scenarios provides valuable insights into the reservoir's behaviour and potential energy production capacity. The sensitivity analysis further enhances the model's utility by identifying the key reservoir parameters that significantly influence the thermal depletion of the reservoir. Overall, this novel modelling approach holds promise for improving the understanding and management of naturally fractured geothermal reservoirs, contributing to the optimization of geothermal energy extraction strategies.

Introduction

Enhanced geothermal systems (EGS) have the potential to increase the supply of geothermal electricity. An EGS functions by forcing water through fractures in hot dry rock, which warms the water. The hot water can then be utilized in a geothermal power plant to produce energy (Breede et al. 2013; Kelkar et al. 2016). Fractured geothermal reservoirs are complex systems that require in-depth understanding and analysis to maximize energy extraction. By delving into the characterization of fracture networks, we can gain insights into the connectivity, orientation, and permeability of the fractures, which play a significant role in the flow of geothermal fluids. To efficiently produce from such reservoirs, a comprehensive understanding of flow behaviour is necessary, which involves integrating various static as well as dynamic geological, geophysical, and engineering data (Azim 2016; Gholizadeh Doonechaly et al. 2016; Hussain et al. 2021). Static data can reveal details on the geometry and orientation of the fracture network. Examples of these data include seismic data, well logs, core descriptions, and borehole images. On the other hand, changes in fracture properties, such as their permeability and roughness, with time can be inferred from dynamic data, such as well test results and production history. These static and dynamic data are utilized as input for reservoir simulation to precisely forecast the behaviour of the fractured reservoir under various production scenarios, contributing to informed decision-making and efficient management. However, including all fractures or fracture networks in standard reservoir simulators is computationally expensive or even technically unfeasible. As a result, numerous studies have been conducted to suggest various methods for representing natural fractures in reservoir simulators (Kazemi 1969; Thomas et al. 1983; Noorishad and Mehran 1982; Sudicky and McLaren 1992; Kim and Deo 2000; Berre et al. 2019). These approaches can be categorized into three groups based on how they address the existence of natural fractures: 1—single-continuum approach, 2—dual continuum approach, and 3—discrete fracture network. A fractured medium can be depicted in single-continuum models (Gupta et al. 2001; Teimoori et al. 2004) as a single continuum with an average permeability that takes the influence of the fractures into account, whereas dual-porosity approach models the matrix and fractures independently by splitting the fractured medium into two continua. The matrix-fracture media interact with each other through transfer functions which control their cross-flow and fluid exchange (Kazemi et al. 1976; Quandalle and Sabathier 1989; Ramirez et al. 2016; Bourbiaux 2010). The discrete fracture (DFN) approach (Sun et al. 2017; Abdel Azim et al. 2023; Gong et al. 2020; Zhou et al. 2022) involves representing each fracture and matrix as 3D tetrahedral elements for the matrix and triangle elements in 2D space for fractures, mathematical flow equations through the matrix and fractures are modelled using various numerical methods such as finite element, finite volume, mixed finite element, and boundary element approaches. Each of these modelling methods has its own strengths and weaknesses. Single-continuum models, while efficient in computation, may not fully represent the complex flow patterns present in fractured reservoirs. Dual-porosity models can depict the distinct flow regimes in the matrix and fractures, but their capacity to depict the intricate interconnectedness of the fracture network is still restricted. DFN models can offer the most comprehensive description of the fracture network, however, implementing this approach is complex with high computational costs due to local refinement requirements during mesh discretization. To address these challenges, this study adopted a hybrid approach where short and long fractures are identified based on a predetermined cut-off value of fracture length. Short fractures are replaced by homogenous grid blocks with an equivalent 3D permeability tensor (i.e., the short fractures are considered as a local spatial heterogeneity within the matrix block) while long fractures are explicitly discretized and coupled with the 3D permeability tensor within the matrix block.

Furthermore, energy extraction from fractured geothermal reservoirs involves a complex interplay of diverse processes, including stress sensitivity, variations in temperature, and rock deformations. These various impacts are commonly combined and referred to as the coupled thermo-hydro-mechanical (THM) process in fractured geothermal reservoirs (Soltani et al. 2019; Olasolo et al. 2016). A fractured geothermal reservoir experiences a decrease in temperature and an increase in pore pressure when water is injected into it. As a result, there is an increase in thermal stress and a decrease in the effective stress in the solid matrix and fractures. These modifications lead to changes in permeability and a widening of the fracture aperture. Therefore, neglecting these mechanical effects will overestimate the amount of thermal recovery from geothermal reservoirs (Zhang and Xie 2020a; Mortazavi et al. 2023). Moreover, it is important to highlight that the impact of chemical reactions, mineral precipitation, and dissolution on the permeability of fracture networks was not taken into account in this study. For further insights into these effects on geothermal reservoirs, readers are referred to studies by Sudicky and Frind (1982); Bolton et al. 1996; Steefel and Lichtner 1998).

The introduction of thermal stress simulation in fractured geothermal reservoirs has been primarily addressed using analytical models and uncoupled approaches. This is due to the complexity of the coupled THM processes involved and the computational challenges associated with simulating these interactions. Analytical models, such as the one developed by Turcotte and Schubert (Turcotte and Schubert 1982), provide a simplified representation of the problem, assuming one-dimensional linear thermo-elasticity. This approach simplifies the calculations and allows for analytical solutions, but it may not capture the full complexity of the reservoir. Uncoupled approaches, where the THM processes are treated separately, have also been widely used. This approach involves solving the governing equations for each process independently and then combining the results to obtain an overall solution. Although this approach is computationally less demanding than fully coupled models, it may not accurately represent the interactions among the THM processes.

The limitations of analytical models and uncoupled approaches have led to the development of more sophisticated numerical models that can capture the full complexity of the THM processes in fractured geothermal reservoirs. These models, such as the ones developed by Zhao et al. (2015); Varnosfaderani et al. 2017; Salimzadeh et al. 2018; Wei et al. 2019; Khoei and Mortazavi 2020; Zhang and Xie 2020b; Li et al. 2021; Wu et al. 2021), use numerical techniques to solve the coupled governing equations, allowing for a more realistic representation of the physical processes involved. These coupled modelling approach provides a valuable tool for evaluating the long-term effects of THM on reservoir properties and present important implications for the development and management of geothermal reservoirs.

Generally speaking, the three main algorithms for modelling THM and multiphase flow in porous media are one-way coupling, iterative coupling, and full coupling. Each approach has its pros and cons, and the choice of algorithm depends on the specific application. One-way coupling involves solving the pressure and displacement equations separately. The pressure equation is first solved, and the resulting pressure field is then input into the displacement equation. This approach is computationally efficient and can be effective in some cases. However, this can also lead to inaccuracies if the coupling between pressure and displacement is strong. Iterative coupling is a more sophisticated approach that iteratively solves the pressure and displacement equations. This approach is more computationally demanding than one-way coupling, but it can provide more accurate results. The iterative coupling method is not based on the Newton–Raphson (N–R) method. The N-R method is a fully coupled and monolithic approach, and its optimum rate of convergence is 2, while the two-way iterative coupling method is at most first-order convergent. Full coupling involves solving the pressure, displacement, and temperature equations simultaneously. This approach is the most computationally demanding of the three, but it can provide the most accurate results. Full coupling is typically used for applications where the coupling between pressure, displacement, and temperature is strong.

In this study, fluid flow simulation is carried out using a hybrid methodology that combines discrete fracture and single continuum approaches using a fully coupled thermo-poro-elastic framework to evaluate the production potential of geothermal reservoirs. In addition, a sensitivity analysis study is carried out to assess the parameters that affect the produced fluid temperature and heat recovery factor. A fracture length less than the threshold value is specified. The periodic boundary method is used to calculate the permeability tensor from fractures that are lower than the threshold value. The reservoir domain is divided into several grid blocks, and in the selected blocks, the single continuum technique is used to simulate fluid flow. In the domain, fractures that are longer than the threshold length are explicitly discretized. The structure of this study is as follow: the derivation of the proposed coupled thermos-poro-elastic mathematical model is presented in "Methodology" section. Then, validation of the in-house simulator against an exact analytical solution of a 2-D thermo-poro-elasticity problem [Kirsch's Problem (Kirsch 1898)], and an application of the in-house model for real field case study of a fractured geothermal reservoir (the Soultz-Sous-Forets geothermal reservoir); are presented in "Results and Discussion" section of this study. Finally, conclusions of the study findings are presented in "Conclusion" section.

Methodology

This study adopted a hybrid approach where short and long fractures are identified based on a predetermined cut-off value of fracture length. Short fractures are replaced by homogenous grid blocks with an equivalent 3D permeability tensor (i.e.; the short fractures are considered as a local spatial heterogeneity within the matrix block). The matrix is discretized using tetrahedral elements in 3D space, while long fractures are explicitly discretized using triangle elements in 2D space.

Effective permeability tensor calculations

Equations (1) and (2), which are based on the assumptions of single-phase and incompressible flow, include Darcy's law and the continuity equations utilized for permeability tensor calculations in a three-dimensional environment:

$$\left\{\begin{matrix} u_x \\ u_y \\ u_z \end{matrix}\right\} = \begin{bmatrix} k_{xx} & k_{xy} & k_{xz} \\ k_{yx} & k_{yy} & k_{yz} \\ k_{zx} & k_{zy} & k_{zz} \end{bmatrix} \left\{\begin{matrix} \frac{\partial p}{\partial x} \\ \frac{\partial p}{\partial y} \\ \frac{\partial p}{\partial z} \end{matrix}\right\} = \overset{\rightrightarrows}{k}.\nabla p \tag{1}$$

$$\nabla.\overrightarrow{\mathbf{u}} = 0.0 \tag{2}$$

where $\overrightarrow{\mathbf{u}}$ is the fluid velocity vector, $[u_x, u_y, u_z]$ are the fluid velocities in x–y– and z directions, $\overrightarrow{\overrightarrow{k}}$ is the permeability tensor and p is the pressure.

Figure 1 shows that each fracture is represented as a 2D triangular element sandwiched between 3D tetrahedral elements that represent the porous matrix (Park and Sung 2000).

Darcy's law is used to simulate fluid flow via a matrix system in a single-phase steady state as follows:

$$\nabla.\left(\frac{\overrightarrow{\overrightarrow{k}}}{\mu}.\nabla p\right) + Q_H = 0.0 \tag{3}$$

$$\vec{\mathbf{u}} = -\left(\frac{\overrightarrow{\overrightarrow{k}}}{\mu}\nabla p\right) \tag{4}$$

where $\overrightarrow{\overrightarrow{k}}$ is the permeability tensor in md, $\mu$is the fluid viscosity in cp, Q_H is the fluid source/sink term, which represents fluid exchange between the matrix and fractures or fluid extraction (injection) from the wellbore, and p is the pressure inside the matrix.

Fluid flow through a single fracture is described by Darcy's law, as shown in the following equation:

$$\overline{\nabla}.\left(\frac{k_f}{\mu}\nabla p_f\right) + q^+ + q^- = 0.0 \tag{5}$$

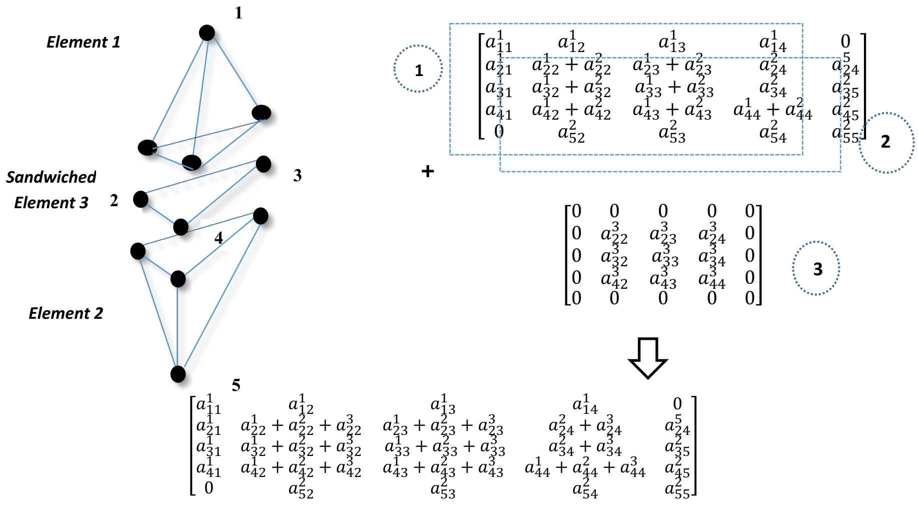

$$\begin{bmatrix} a_{11}^1 & a_{12}^1 & a_{13}^1 & a_{14}^1 & 0 \\ a_{21}^1 & a_{22}^1 + a_{22}^2 & a_{23}^1 + a_{23}^2 & a_{24}^2 & a_{24}^5 \\ a_{31}^1 & a_{32}^1 + a_{32}^2 & a_{33}^1 + a_{33}^2 & a_{34}^2 & a_{35}^2 \\ a_{41}^1 & a_{42}^1 + a_{42}^2 & a_{43}^1 + a_{43}^2 & a_{44}^1 + a_{44}^2 & a_{45}^2 \\ 0 & a_{52}^2 & a_{53}^2 & a_{54}^2 & a_{55}^2 \end{bmatrix}$$

$$\begin{bmatrix} 0 & 0 & 0 & 0 & 0 \\ 0 & a_{22}^3 & a_{23}^3 & a_{24}^3 & 0 \\ 0 & a_{32}^3 & a_{33}^3 & a_{34}^3 & 0 \\ 0 & a_{42}^3 & a_{43}^3 & a_{44}^3 & 0 \\ 0 & 0 & 0 & 0 & 0 \end{bmatrix}$$

$$\begin{bmatrix} a_{11}^1 & a_{12}^1 & a_{13}^1 & a_{14}^1 & 0 \\ a_{21}^1 & a_{22}^1 + a_{22}^2 + a_{22}^3 & a_{23}^1 + a_{23}^2 + a_{23}^3 & a_{24}^2 + a_{24}^3 & a_{24}^5 \\ a_{31}^1 & a_{32}^1 + a_{32}^2 + a_{32}^3 & a_{33}^1 + a_{33}^2 + a_{33}^3 & a_{34}^2 + a_{34}^3 & a_{35}^2 \\ a_{41}^1 & a_{42}^1 + a_{42}^2 + a_{42}^3 & a_{43}^1 + a_{43}^2 + a_{43}^3 & a_{44}^1 + a_{44}^2 + a_{44}^3 & a_{45}^2 \\ 0 & a_{52}^2 & a_{53}^2 & a_{54}^2 & a_{55}^2 \end{bmatrix}$$

Fig. 1 Schematic diagram and workflow illustrating how the 3D matrix for the fractured system was created for use in the simulation. Fracture is represented as (Sandwich elements) between 3-D tetrahedral matrix elements (Elements 1&2) assembled to be used during the simulation process where q^{+} and q^{-} are the leakage fluxes across the boundary interface, $\overline{\nabla}$ is the divergence operator in the local coordinate system (Watanabe et al. 2010a) and P_f is the pressure inside the fracture.

Since it was assumed in this study that the fracture surface is uniform and that fluid flow through a single discrete fracture is laminar, the permeability of the fracture is represented by the cubic law (Snow 1969):

$$k_f = \frac{b^2}{12} \tag{6}$$

where *b* is the fracture aperture and k_f is the fracture permeability.

The weak formulations of fluid flow through a fractured system are derived using a weighted residual approach, and the weak forms are then discretized with suitable boundary conditions using the conventional Galerkin method (Snow 1969). Following the superimposition of the flux contributions from both the matrix and fracture element types at each node, the fluid exchange terms q + and q- balance, opposing the need for explicit computations (Zienkiewicz and Taylor 2000). Equations 3 and 4 are written separately for the matrix and fractured media. The matrix will be discretized in 3D form, and fractures will be discretized in 2D form.

For the fluid exchange terms q + and q- to balance, the following must be true:

- The incoming and outgoing fluxes at each node are equal, resulting in no net accumulation or depletion of fluid at any point.
- The matrix and fractures are perfectly connected, allowing fluid to flow freely between them in both directions.
- The fluxes of q + and q- are equal at each node, indicating a state of equilibrium in terms of fluid exchange between the matrix and fractures.

*C*FEQ represents the control flow Eqs. (3) and (4). The integral of these equations for the discrete fracture model is written as

$$\int\!\!\int_{\Omega} \mathrm{CFEQ}\, d\Omega = \int\!\!\int_{\Omega_m} \mathrm{CFEQ}\, d\Omega_m + b \int\!\!\int_{\Omega_f} \mathrm{CFEQ}\, d\overline{\Omega}_f \tag{7}$$

$\overline{\Omega}_f$ indicates the 2D entity that is the fracture portion of the domain, and Ω_m stands for the matrix domain; the entire domain is represented by Ω, the integral form of the 2D fracture equation is consistent when it is multiplied by the fracture aperture b. One way to express the hydraulic process's governing equation in matrix and fracture system form using finite elements is as follows:

$$\left[\vec{\vec{M}}\right]\left[\overrightarrow{\Delta p}\right] = \vec{f} \tag{8}$$

$$\vec{\vec{M}} = \vec{\vec{M}}{}_1^m + \vec{\vec{M}}{}_2^f \tag{9}$$

$$\vec{\vec{M}} = \int_{\Omega} \nabla N_p^{m^T} \frac{k}{\mu} \nabla N_p^m d\Omega + \int_{\Gamma} \nabla N_p^{f^T} \left(\frac{bxk}{\mu}\right) \nabla N_p^f d\Gamma \tag{10}$$

$$\vec{f} = -\int\limits_{\Gamma} N_p^{m^T} Q_H \, d\Gamma - \vec{\vec{M}}_1^m \vec{P}^{i-1m} - \vec{\vec{M}}_2^f \vec{P}^{i-1f} - \int\limits_{\Gamma} N_p^{f^T} Q_H \, d\Gamma \tag{11}$$

where ***N*** is the corresponding shape function for the matrix and fracture elements and Γ is a domain boundary.

Upscaling using periodic boundary conditions

Equation (1) uses the periodic boundary conditions presented by (Durlofsky 1991) to solve the permeability tensor's elements. Equations (12) through (17) specify the pressure and flux boundaries, as Fig. 2 illustrates:

$$P\ (y,\ x = 0,\ z)\ =\ P\left(y,\ x = 1,\ z\right)\ - \mathbf{G}n\, \partial\Gamma_3 \text{ and } \partial\Gamma_4 \tag{12}$$

$$u\ (y,\ x = 0,\ z).\mathbf{n_3} = -u\left(y,\ x = 1,\ z\right).\mathbf{n_4} \quad \text{on } \partial\Gamma_3 \text{ and } \partial\Gamma_4 \tag{13}$$

$$P\left(y = 0,\ x,\ z\right)\ =\ P\left(y = 1,\ x,\ z\right) \quad \text{on } \partial\Gamma_1 \text{ and } \partial\Gamma_2 \tag{14}$$

$$u\left(y = 0,\ x,\ z\right)^{\cdot}\mathbf{n_1} = -u\left(y = 1,\ x,\ z\right)^{\cdot}\mathbf{n_2} \quad \text{on } \partial\Gamma_1 \text{ and } \partial\Gamma_2 \tag{15}$$

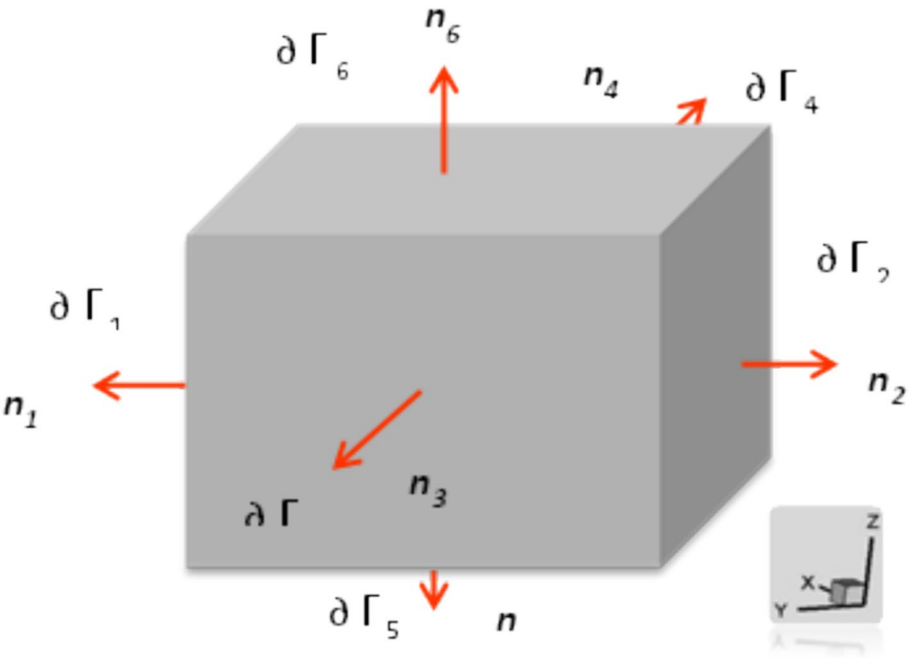

Fig. 2 Single-phase flow model is utilized to compute the elements of the permeability tensor in three dimensions with periodic boundary conditions

$$\mathrm{P}\left(\mathrm{y},\ \mathrm{x},\ \mathrm{z}=0\right)\ =\ \mathrm{P}\left(\mathrm{y},\ \mathrm{x},\ \mathrm{z}=1\right)\quad \text{on } \partial\Gamma_5 \text{ and } \partial\Gamma_6 \tag{16}$$

$$\mathrm{u}\left(\mathrm{y},\ \mathrm{x},\ \mathrm{z}=0\right)^{\cdot}\mathbf{n_5}=-\mathrm{u}\left(\mathrm{y},\ \mathrm{x},\ \mathrm{z}=1\right).\mathbf{n_6}\quad \text{on } \partial\Gamma_6 \text{ and } \partial\Gamma_6 \tag{17}$$

where ***n*** is the outwards normal vector at the boundaries, Γ is the domain boundary, and **G** is the pressure gradient.

First, by assuming a zero-pressure gradient (G = 0.0) along the y and z directions and by solving Eq. 8 subject to Eqs. (12)–(17), the average velocities along the x, y and z directions are calculated via Eqs. (18)–(20):

$$\mathrm{u_x}=-\int_{\partial\Gamma3}\mathrm{v.n_3dx\,dz} \tag{18}$$

$$\mathrm{u_y}=-\int_{\partial\Gamma1}\mathrm{v.n_1dy\,dz} \tag{19}$$

$$\mathrm{u_z}=-\int_{\partial\Gamma5}\mathrm{v.n_5dx\,dy} \tag{20}$$

Equation (1) is expressed in an explicit form as follows:

$$\mathrm{u_x}=-\mathrm{k_{xx}}\frac{\partial \mathrm{p}}{\partial \mathrm{x}}-\mathrm{k_{xy}}\frac{\partial \mathrm{p}}{\partial \mathrm{y}}-\mathrm{k_{xz}}\frac{\partial \mathrm{p}}{\partial \mathrm{z}} \tag{21}$$

$$\mathrm{u_y}=-\mathrm{k_{yx}}\frac{\partial \mathrm{p}}{\partial \mathrm{x}}-\mathrm{k_{yy}}\frac{\partial \mathrm{p}}{\partial \mathrm{y}}-\mathrm{k_{yz}}\frac{\partial \mathrm{p}}{\partial \mathrm{z}} \tag{22}$$

$$\mathrm{u_z}=-\mathrm{k_{zx}}\frac{\partial \mathrm{p}}{\partial \mathrm{x}}-\mathrm{k_{zy}}\frac{\partial \mathrm{p}}{\partial \mathrm{y}}-\mathrm{k_{zz}}\frac{\partial \mathrm{p}}{\partial \mathrm{z}} \tag{23}$$

where $\mathrm{u_x}$, $\mathrm{u_y}$ and $\mathrm{u_z}$ are the velocities in the x, y, and z directions, respectively. Since the pressure gradient in the y and z directions is assumed to be zero and $\mathrm{u_x}$, $\mathrm{u_y}$ and $\mathrm{u_z}$ are known, $\mathrm{k_{xx}}$, $\mathrm{k_{yx}}$ and $\mathrm{k_{zx}}$ can be easily determined.

The rest of the permeability tensor elements can be calculated by using the same boundary conditions as mentioned above but in other directions.

Fluid flow in long fractures (with a length greater than the threshold length) is coupled with an element-based permeability tensor in a poroelastic environment. A finite element technique is used in this study to formulate governing equations for hydraulic and mechanical processes (poroelastic processes). The coupled form of the fluid momentum equation is presented below:

$$\nabla.\left(\frac{\vec{\vec{\mathrm{k}}}}{\mu}.\nabla \mathrm{p}\right)=\phi \mathrm{c_t}\frac{\partial \mathrm{p}}{\partial \mathrm{t}}-\alpha'\frac{\partial}{\partial \mathrm{t}}(\nabla.\vec{\mathrm{u}})+\mathrm{Q} \tag{24}$$

where u is the displacement vector in three-dimensional space, $\mathrm{c_t}$ is the total compressibility (1/psi), α' is the Biot constant and ϕ is the porosity. The equation for describing fluid flow through a matrix in the finite element method is expressed as follows:

Introducing the weak formulation, Eq. (24) for fluid flow through the matrix is described as follows:

$$\begin{aligned}&\int_{\Omega} \mathbf{w}\phi c_t \frac{\partial p}{\partial t} d\Omega - \int_{\Omega} \mathbf{w}\alpha' \frac{\partial}{\partial t}\left(\frac{\partial}{\partial x}\frac{\partial}{\partial y}\frac{\partial}{\partial z}\right)\vec{u}\, d\Omega \\ &= \int_{\Omega} \mathbf{w}\left(\frac{\partial}{\partial x}\left(\frac{k_{xx}}{\mu}\frac{\partial p}{\partial x}+\frac{k_{xy}}{\mu}\frac{\partial p}{\partial y}+\frac{k_{xz}}{\mu}\frac{\partial p}{\partial z}\right)+\frac{\partial}{\partial y}\left(\frac{k_{yx}}{\mu}\frac{\partial p}{\partial x}+\frac{k_{yy}}{\mu}\frac{\partial p}{\partial y}+\frac{k_{yz}}{\mu}\frac{\partial p}{\partial z}\right)\right. \\ &\quad \left.+\frac{\partial}{\partial z}\left(\frac{k_{zx}}{\mu}\frac{\partial p}{\partial x}+\frac{k_{zy}}{\mu}\frac{\partial p}{\partial y}+\frac{k_{zz}}{\mu}\frac{\partial p}{\partial z}\right)\right)d\Omega + \int_{\Gamma} w^{T}\, q\, d\Gamma\end{aligned} \tag{25}$$

where ($\boldsymbol{w} = \boldsymbol{w}$ (x, y, z)) is a trial function.

Using the finite-element method for discretization with respect to time and space results in

$$\begin{aligned}&\int_{\Omega}\left(\phi c_t N_p^T N_p d\Omega\right)\left(\vec{P}^{\,i} - \vec{P}^{\,i-1}\right) - \left[\left(\int_{\Omega} N_p^T\, \alpha'\left(\frac{\partial}{\partial x}\,\frac{\partial}{\partial y}\,\frac{\partial}{\partial z}\right)N_u\right)d\Omega\right]\left(\vec{U}^{\,i} - \vec{U}^{\,i-1}\right) \\ &+\Delta t^{i}\left[\int_{\Omega}\left(\frac{k_{xx}}{\mu}\frac{\partial N_p^T}{\partial x}\frac{\partial N_p}{\partial x}+\frac{k_{xy}}{\mu}\frac{\partial N_p^T}{\partial x}\frac{\partial N_p}{\partial x}+\frac{k_{xz}}{\mu}\frac{\partial N_p^T}{\partial x}\frac{\partial N_p}{\partial x}\right)d\Omega\right]\vec{P}^{\,i} \\ &+\Delta t^{i}\left[\int_{\Omega}\left(\frac{k_{yx}}{\mu}\frac{\partial N_p^T}{\partial y}\frac{\partial N_p}{\partial y}+\frac{k_{yy}}{\mu}\frac{\partial N_p^T}{\partial y}\frac{\partial N_p}{\partial y}+\frac{k_{yz}}{\mu}\frac{\partial N_p^T}{\partial y}\frac{\partial N_p}{\partial y}\right)d\Omega\right]\vec{P}^{\,i} \\ &+\Delta t^{i}\left[\int_{\Omega}\left(\frac{k_{zx}}{\mu}\frac{\partial N_p^T}{\partial z}\frac{\partial N_p}{\partial z}+\frac{k_{zy}}{\mu}\frac{\partial N_p^T}{\partial z}\frac{\partial N_p}{\partial z}+\frac{k_{zz}}{\mu}\frac{\partial N_p^T}{\partial z}\frac{\partial N_p}{\partial z}\right)d\Omega\right]\vec{P}^{\,i} + \int_{\Gamma} N_p^T q\, d\Gamma = 0.0\end{aligned} \tag{26}$$

where

$$\vec{P}^{\,T} = (P_1\, P_1 \ldots\ldots\ldots\ldots P_n)$$

$$\vec{U}^{\,T} = \left(u_{x1}\, u_{y1}\, u_{z1}\, \ldots\ldots\ldots\ldots u_{zn}\right)$$

$N_{p}andN_{u}$ are the shape functions for pressure and displacement, respectively; $\boldsymbol{n}$ is the number of nodes; Γ is the domain boundary; and *u* and P are the nodal values of displacement and pressure, respectively.

Equation (25) for fluid flow through discrete fractures is described as follows:

$$\begin{aligned}&\int_{\Omega}\left(\phi c_t N_p^{f^T} N_p^f d\Omega\right)\left(\vec{P}^{\,i} - \vec{P}^{\,i-1}\right) - \left[\left(\int_{\Omega} N_p^{f^T}\alpha'\left(\frac{\partial}{\partial x}\frac{\partial}{\partial y}\frac{\partial}{\partial z}\right)N_u\right)d\Omega\right]\left(\vec{U}^{\,i} - \vec{U}^{\,i-1}\right) \\ &+\Delta t^{i}\left[\int_{\Omega}\left(\nabla N_p^{f^T}\frac{k_f}{\mu}\nabla N_p^f\right)d\Omega\right]\vec{P}^{\,i} + \int_{\Gamma_f} N_p^{f^T} q\, d\Gamma_f = 0.0\end{aligned} \tag{27}$$

where $N^f andN_u$ are the shape functions for pressure and displacement, respectively, for the fracture domain; Γ_f and is the fracture boundary domain; and *u* and P are the displacement and pressure fracture nodal values, respectively.

The integration of discrete fracture spaces requires a coordinate transformation (Watanabe et al. 2010a).

Coordinate transformation

The coordinates of fractures should be transformed from local coordinates to global coordinates by using the rotational matrix **R**.

where S is the vector of global coordinates (x–y–z) and S' is the vector of local coordinates ($x^{'}$-$y^{'}$-$z^{'}$). The transformation from local to global coordinates is as follows:

$$S = RS' \tag{28}$$

where

$$R = \begin{bmatrix} Cos(x',x)Cos(x',y)Cos(x',z) \\ Cos(y',x)Cos(y',y)Cos(y',z) \\ Cos(z',x)Cos(z',y)Cos(z',z) \end{bmatrix} \tag{29}$$

where Cos(x', x) is the angle between the axes x', x.

Permeability tensor transformation

An evaluation of the permeability tensor in appropriate coordinate systems is necessary. The permeability in local coordinates can be transformed into global coordinates as follows:

$$k = RkR^T \tag{30}$$

where k and $k^{'}$ are the permeabilities in global and local coordinates, respectively.

Shape function transformation

Fracture shape functions can be transformed into global coordinates as follows:

$$N = RN'R^T \tag{31}$$

where N and $N^{'}$ are the shape functions in global and local coordinates, respectively.

Thermo-poroelastic coupled model

The following are the governing constitutive equations for the conservation of mass, momentum, and energy. The momentum balance equation for the linear elastic deformations can be written as

$$\nabla \cdot \sigma + \rho g = 0 \tag{32}$$

where ρ is the density of the porous medium, which can be written as in Eq. (33), and g is the gravity constant:

$$\boldsymbol{\rho = \varphi \rho_l + (1 - \varphi)\rho_s} \tag{33}$$

In addition, Eq. (32) can be written in terms of the effective stress as follows:

$$\nabla \cdot \left(\sigma' - pI\right) + \rho g = 0 \tag{34}$$

where σ' is the effective stress, p is the pore pressure, and I is the identity matrix:

$$d\sigma' = D\left(d\varepsilon - d\varepsilon^{T}\right) \tag{35}$$

$$\sigma' = C(\varepsilon - \alpha_T \Delta T \times I) \tag{36}$$

where D is the operator matrix (Zienkiewicz 2000), ε^{T} is the thermal strain, ε is the total strain, α_T is the thermal expansion coefficient, ΔT is the temperature difference and C is the fourth-order material tensor, as shown in the following equation:

$$C = \lambda\delta_{ij}\delta_{kl} + 2G\delta_{ik}\delta_{jl} \tag{37}$$

In Eq. (37), δ is the Kronecker delta function, G is the shear modulus of elasticity, and λ is the Lame coefficient:

$$\boldsymbol{\varepsilon} = \frac{1}{2}\left(\nabla \boldsymbol{u} + (\nabla \boldsymbol{u})^{\mathrm{T}}\right) \tag{38}$$

The mass balance equation for the fluid phase in a deformable non-isothermal porous medium describes the conservation of mass of the fluid within the porous medium as it deforms and experiences temperature changes. It is a fundamental equation used to model and analyse fluid flow and heat transfer in geothermal reservoirs, subsurface hydrology, and other applications involving fluid flow in porous media.

The mass balance equation for the fluid phase can be expressed as follows:

$$S_s\frac{\partial p}{\partial t} + \nabla\cdot q + \nabla\cdot\left(\frac{\partial u}{\partial t}\right) - \alpha_T\frac{\partial T}{\partial t} = Q \tag{39}$$

where α_T is the thermal expansion coefficient, T is the temperature, q is the fluid flux, Q is the sink/source term, and S is the specific storage, which is given in Eq. (40):

$$S = \left(\frac{1-\varphi}{K_s}\right) + \left(\frac{\varphi}{K_l}\right) \tag{40}$$

$$q = -\frac{k}{\mu}(\nabla p - \rho g) \tag{41}$$

Introducing Eqs. (40) and (40) into Eq. (39) results in the following equation:

$$\left[\left(\frac{1-\varphi}{K_s}\right) + \left(\frac{\varphi}{K_l}\right)\right]\frac{\partial p}{\partial t} + \nabla\cdot\left(\frac{\partial u}{\partial t}\right) - \alpha_T\frac{\partial T}{\partial t} + \nabla^{T}\left[-\frac{k}{\mu}(\nabla p - \rho g)\right] = 0 \tag{42}$$

The thermal expansion coefficient α_T of the medium is given in Eq. (43) and can be calculated with the following formula:

$$\alpha_T = (1-\varphi)\alpha_{T_{solid}} + \varphi\alpha_{T_{liquid}} \tag{43}$$

where φ is the porosity of the medium, $\alpha_{T_{solid}}$ is the thermal expansion coefficient of the solid phase and $\alpha_{T_{liquid}}$ is the thermal expansion coefficient of the liquid phase.

The energy balance equation for a saturated porous medium describes the conservation of energy within the porous medium as it undergoes temperature changes and fluid flow. It is a fundamental equation used to model and analyse heat transfer in geothermal reservoirs, subsurface hydrology, and other applications involving heat transport in porous media.

The form of the energy balance equation for a saturated porous medium is

$$(\rho c_p)_{eff}\frac{\partial T}{\partial t} + \nabla.qT = Q_T \tag{44}$$

where $(\rho c_p)_{eff}$ is the effective heat storage of the porous medium, which is defined in Eq. (45); q is the heat flux; and Q_T is the heat sink/source term:

$$(\rho c_p)_{eff} = \varphi(c_p\rho)_{liquid} + (1-\varphi)(c_p\rho)_{solid} \tag{45}$$

In addition, this analysis takes into account both convection and conduction heat fluxes, which allows us to write the heat flux term in Eq. (46) as follows:

$$Q_T = -\lambda_{eff}\nabla T + (c_p\rho)_{liquid}v\cdot T \tag{46}$$

where λ_{eff} is the effective heat conductivity of the porous medium, which can be defined as Eq. (47), and v is the velocity of the fluid:

$$\lambda_{eff} = \varphi\lambda_{liquid} + (1-\varphi)\lambda_{solid} \tag{47}$$

By introducing Darcy's law into Eq. (44), the general energy conservation

$$(\rho c_p)_{eff}\frac{\partial T}{\partial t} + \left[(c_p\rho)_{liquid}\times\frac{k}{\mu}\times(-\nabla p+\rho g)\right]\cdot\nabla T - \nabla^T(\lambda_{eff}\nabla T) = Q \tag{48}$$

In this study, the basic two-equation model for local thermal nonequilibrium heat transfer is used in a numerical thermo-poroelastic framework to consider the effect of LTNE on estimating potential recoverable energy from geothermal reservoirs. For this purpose, the continuous solid model is used (Demirel 2007). The two-equation model for the solid/liquid phases is expressed as

$$\left.\frac{\partial T}{\partial t}\right|_f + v\cdot\nabla T_f = \left[h_{sf}\times\frac{A_s}{\varphi\times(\rho c_p)_f}\times(T_s-T_f)\right] + \nabla^T(\lambda_f\nabla T) \tag{49}$$

$$\left.\frac{\partial T}{\partial t}\right|_s = \left[h_{sf}\times\frac{A_s}{(1-\varphi)\times(\rho c_p)_s}\times(T_f-T_s)\right] + \nabla^T(\lambda_s\nabla T) \tag{50}$$

where h_{sf} is the heat transfer coefficient between the solid and the liquid phases, A_s is the specific surface area, φ is the porosity of the porous medium, T_f and T_s are the fluid and the solid temperature at the fluid/solid interface, λ is the heat conductivity and ρc_p is the heat storage of the corresponding medium. As shown in Eqs. (49) and (50), heat transfer is assumed to occur by conduction in the solid phase and by conduction and convection in the liquid phase. The axial conduction in both phases is also included in the calculation using the thermal conductivities of both the solid and liquid phases (λ), Table 1.

Table 1 Typical range of reservoir data for Soultz geothermal reservoir used for the fluid flow and heat transfer simulation (Kohl et al. 1995; Baria et al. 1999; Andre et al. 2006; Tenzer et al. 2010; Watanabe et al. 2010b; Koh et al. 2011)

Rock Properties	
Young's modulus (GPa)	40
Poisson's ratio	0.3
Density (Kg/m^3)	2700
Matrix permeability (m^2)	9.8×10^{-18}
Stress data	
Vertical stress (MPa)	40
Maximum horizontal stress (MPa)	40
Minimum horizontal stress (MPa)	38
Fluid Properties	
Viscosity (Pa s)	2×10^{-4}
Compressibility (MPa^{-1})	2.5×10^{-8}
Density (Kg/m^3)	1000
Injector Temp, stimulation (K)	350
Injector pressure, production (MPa)	38
Producer pressure, production (MPa)	7
Producer temp, production (K)	320
Reservoir data	
Wellbore radius (m)	0.1
Reservoir depth (m)	4065
Specific heat (rock) (Jkg^{-1} K^{-1})	1.098×10^3
Specific heat (fluid) (Jkg^{-1} K^{-1})	4.05×10^3
Thermal Conductivity (rock) (Wm^{-1} s^{-1})	3.58
Thermal Conductivity (fluid) (Wm^{-1} s^{-1})	0.62

To discretize the abovementioned mass, momentum and energy conservation equations, the weighted residual method and Green's theorem are applied (Bathe 1996):

$$u = N_u \overline{u} \tag{51}$$

$$p = N_p \overline{p} \tag{52}$$

$$T = N_T \overline{T} \tag{53}$$

where N is the corresponding shape function and $\overline{u}$, $\overline{p}$ and $\overline{T}$ are the nodal values of the corresponding state variables. By applying Galerkin's method and replacing the weighting functions with the shape functions of the corresponding variables, the weak form of the conservation equations can be written as follows:

$$\begin{aligned}\int_{\Omega} wS_s \frac{\partial p}{\partial t} d\Omega + \int_{\Omega} w^T \alpha \nabla \cdot \frac{\partial u}{\partial t} d\Omega + \int_{\Omega} w\beta \frac{\partial T}{\partial t} - \int_{\Omega} \nabla w^T \cdot q_H d\Omega \\ + \int_{\Gamma_H^q} w(q_H \cdot n) d\Gamma - \int_{\Omega} wQ_H d\Omega = 0\end{aligned} \tag{54}$$

$$\begin{aligned}&\int_{\Gamma_d} wb_m S_s \frac{\partial p}{\partial t} d\Gamma + \int_{\Gamma_d} w\alpha \frac{\partial b_m}{\partial t} d\Gamma + \int_{\Gamma_d} w\beta \frac{\partial T}{\partial t} d\Gamma - \int_{\Gamma_d} \nabla w^T \cdot (b_h q_H) d\Omega \\ &+ \int_{\Gamma_H^q} wb_h (q_H \cdot n) d\Gamma + \int_{\Gamma_d} wq_H^+ d\Gamma + \int_{\Gamma_d} wq_H^- d\Gamma = 0\end{aligned} \tag{55}$$

$$\begin{aligned}&\int_{\Omega} wc_p\rho \frac{\partial T}{\partial t} d\Omega + \int_{\Omega} wc_p\rho q_H \cdot \nabla T d\Omega - \int_{\Omega} \nabla w^T \cdot (-\lambda \nabla T) d\Omega \\ &+ \int_{\Gamma_T^q} w(-\lambda \nabla T \cdot n) d\Gamma - \int_{\Omega} w^T Q_T d\Omega = 0\end{aligned} \tag{56}$$

$$\begin{aligned}&\int_{\Gamma_d} wb_m c_p^l \rho^l \frac{\partial T}{\partial t} d\Gamma + \int_{\Gamma_d} wc_p^l \rho^l b_h q_H \cdot \nabla T d\Gamma - \int_{\Gamma_d} \nabla w^T \cdot (-b_m \lambda^l \nabla T) d\Gamma \\ &+ \int_{\Gamma_T^q} w(-b_m \lambda^l \nabla T \cdot n) d\Gamma + \int_{\Gamma_d} wq_T^+ d\Gamma + \int_{\Gamma_d} q_T^- d\Gamma = 0\end{aligned} \tag{57}$$

$$\int\limits_{\Omega} \nabla^s w^T \cdot \left(\sigma' - \alpha p I\right) d\Omega - \int\limits_{\Omega} w^T \cdot \rho g d\Omega - \int\limits_{\Gamma_t} w^T \cdot \bar{t} d\Gamma - \int\limits_{\Gamma_d} w^{+T} \cdot t_d^+ d\Gamma - \int w^{-T} \cdot t_d^- d\Gamma = 0 \tag{58}$$

where w is the test function, Ω is the model domain, Γ is the domain boundary, t is the traction vector and d is the fracture plane.

Using the Galerkin weighted residual method and the implicit finite difference method for time discretization, the finite element formulation of the field equations is given by

$$\begin{bmatrix} K & Q & -W \\ Q^T & -(F + \Delta t H_F) & -(C + \Delta t H_T) \\ 0 & 0 & -(M + \Delta t H_D) \end{bmatrix} \begin{bmatrix} \Delta \overrightarrow{U}^i \\ \Delta \overrightarrow{P}^i \\ \Delta \overrightarrow{T}^i \end{bmatrix} = \begin{bmatrix} \Delta f \\ \Delta t H_F p(t_{i-1}) + \Delta t H_T T(t_{i-1}) \\ \Delta t H_D p(t_{i-1}) \end{bmatrix} \tag{59}$$

where i is the time step and

$$\begin{aligned}&\overrightarrow{\Delta P} = \overrightarrow{P^i} - \overrightarrow{P^{i-1}}, \overrightarrow{\Delta U} = \overrightarrow{U^i} - \overrightarrow{U^{i-1}} \\ &\overrightarrow{\Delta T} = \overrightarrow{T^i} - \overrightarrow{T^{i-1}}\end{aligned} \tag{60}$$

$$K = \int\limits_{\Omega} B^T D B d\Omega \tag{61}$$

$$Q = \int\limits_{\Omega} B^T \alpha_T N_P d\Omega \tag{62}$$

$$W = \int\limits_{\Omega} B^T \alpha N_P d\Omega \tag{63}$$

$$F = \int_{\Omega} N_P^T S N_P d\Omega \tag{64}$$

$$H_F = \int_{\Omega} (\Delta N_P)^T k (\Delta N_P) d\Omega \tag{65}$$

$$C = \int_{\Omega} N_P^T \beta N_P d\Omega \tag{66}$$

$$H_T = \int_{\Omega} (\Delta N_P)^T \alpha^T (\Delta N_P) d\Omega \tag{67}$$

$$M = \int_{\Omega} N_T^T (\rho c)_s N_T d\Omega \tag{68}$$

$$H_D = \int_{\Omega} (\Delta N_P)^T \lambda_{eff} (\Delta N_T) d\Omega - (\Delta N_T)^T (\rho c)_f \left(\frac{k}{\mu} \times \left(-\nabla p + \rho g \right) \right) (\Delta N_T) d\Omega \tag{69}$$

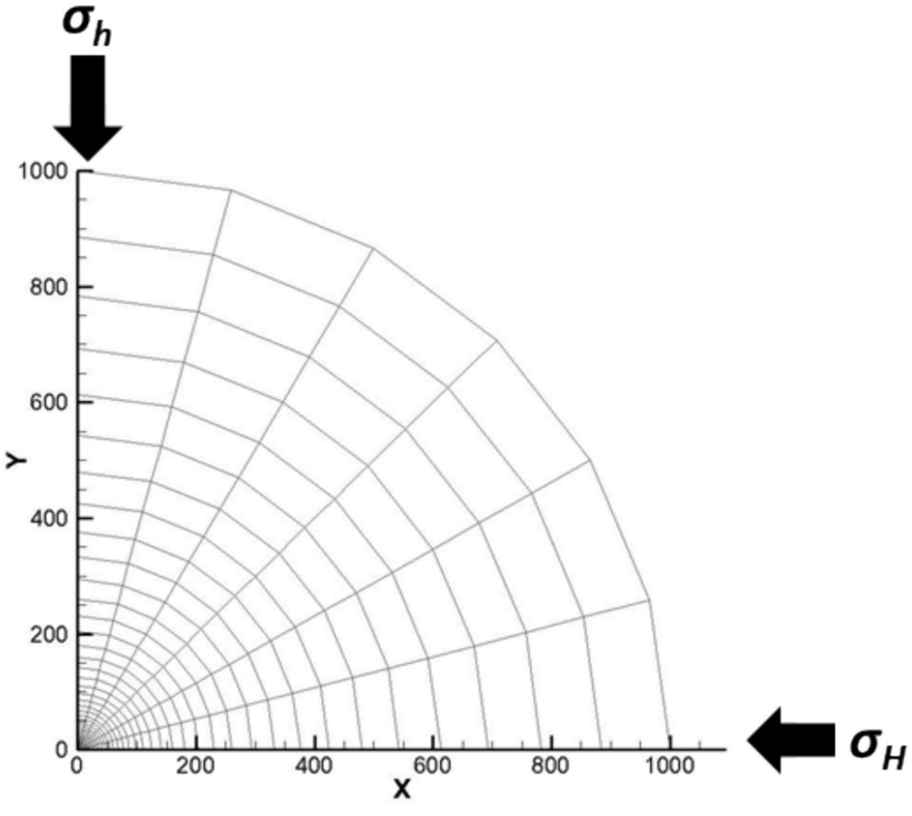

Fig. 3 Two dimensions Circular reservoir shape used for validation of Thermo poroelastic numerical model with $\sigma_H = 40$ MPa and $\sigma_h = 38$ MPa, $P_{inj} = 38$ MPa, $P_{pro} = 7$ MPa, $T_s = 350$ °K, Ti = 320 °K

Table 2 Typical range of reservoir data for Soultz geothermal reservoir used for the fluid flow and heat transfer simulation (Kohl et al. 1995; Baria et al. 1999; Andre et al. 2006; Tenzer et al. 2010; Watanabe et al. 2010b; Koh et al. 2011)

	Value
Rock properties	
Rock Young's modulus (GPa)	42
Rock Poisson's ratio	0.26
Water density (kg/m^3)	2700
Matrix permeability (m^2)	32×10^{-16}
Coefficient of heat transfer (W/m^2.K)	0.8
Fracture properties	
Reservoir fractal dimension, D	1.3
Reservoir fracture density (m^2/m^3)	0.18
Minimum fracture radius (m)	10
Maximum fracture radius (m)	175
Stress data	
Minimum horizontal stress (MPa)	17
Maximum horizontal stress (MPa)	55
Vertical stress (MPa)	57
Fluid properties	
Density (kg/m^3)	1000
Viscosity (Pa.s)	3×10^{-4}
Injector well pressure (MPa)	42
Producer well pressure (MPa)	31.7
Other reservoir data	
Well radius (m)	0.1
Number of injector wells	1
Number of producer wells	1
Reservoir thickness (m)	100
Rock specific heat (Jkg^{-1} K^{-1})	1.2×10^3
Fluid specific heat (Jkg^{-1} K^{-1})	3.5×10^3
Rock thermal conductivity (Wm^{-1} s^{-1})	2.258
Fluid thermal conductivity (Wm^{-1} s^{-1})	0.78

D is the anisotropic drained elastic stiffness tensor, B is Skempton coefficient, NP is a pressure shape function, α is Biot's coefficient, and k is the permeability.

According to the fundamentals of poro-elasticity, porosity is related to the average effective stress σ_{ii} and the shear modulus of the solid phase G_s. ϕ_o is the porosity in the unstressed state:

$$\phi = \phi_o e^{(\sigma_{ii}/4G_s)} \tag{70}$$

Permeability is considered to be a stress-independent functional relationship, so Eq. (71) indicates the exponential function for the absolute flow permeability considering porosity changes:

$$k = \lambda k_o \tag{71}$$

where k_o is the initial permeability and k is the current permeability under nonzero stress conditions. The λ parameter is a function of porosity and can be expressed by

$$\lambda = \left(\frac{\phi}{\phi_o}\right)^3 \left(\frac{1-\phi_o}{1-\phi}\right)^2 \tag{72}$$

Results and discussion

Validation of thermo-poro-elastic numerical model using Kirch's problem

The verification of thermos-poro-elastic numerical model against analytical solutions is presented in this section. A 2D model of circular shaped reservoir with an intact wellbore is used during the validation process. The model is presented in Fig. 3 with reservoir drainage radius of 1000 m and wellbore radius of 0.1 m. The reservoir input data used is presented in Table 2. The numerical model is initiated with drained conditions and these conditions obtained by using Kirsh's problem. The analytical solution of thermal stress is presented in the following formulas:

Analytical temperature

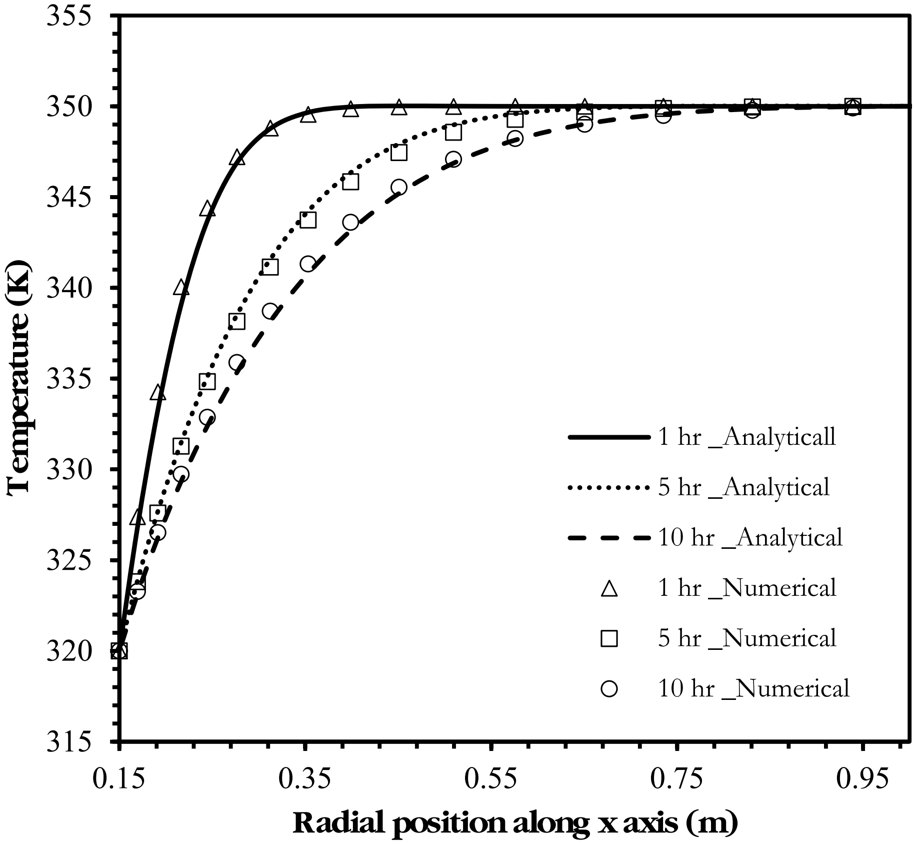

Fig. 4 Rock temperature as a function of time and radius in poroelastic medium with $\sigma_H = 40$ MPa psi and $\sigma_h = 38$ MPa, $P_{inj} = 38$ MPa, $P_{pro} = 7$ MPa, $T_s = 350\ ^{o}K$, $T_i = 320\ ^{o}K$

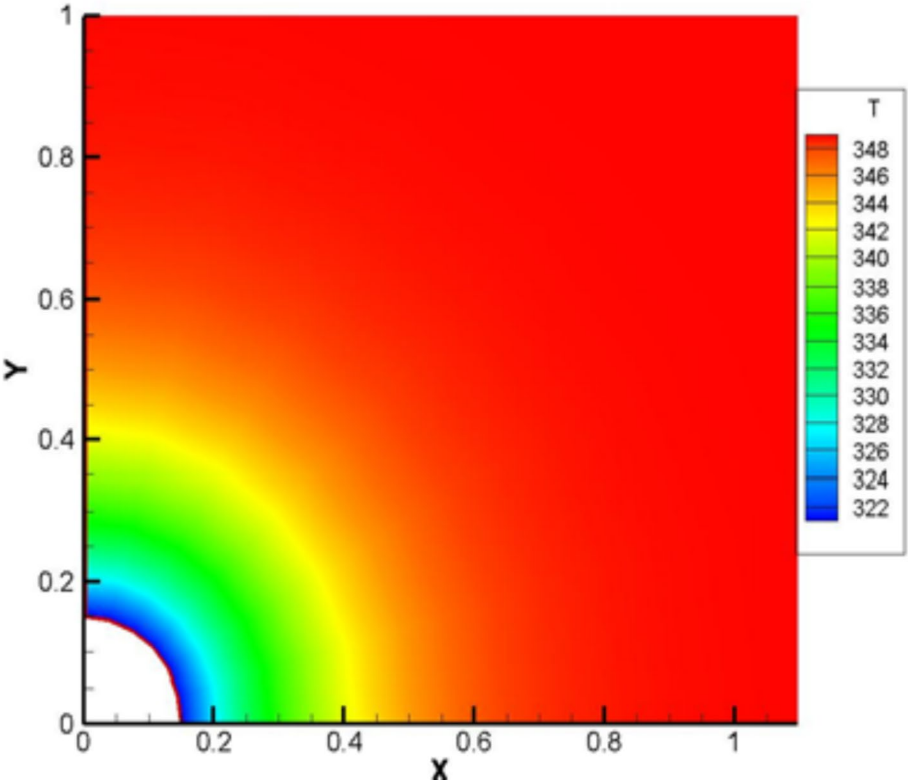

Fig. 5 Rock temperature contour map after 1 h of fluid production with $\sigma_H = 40$ MPa psi and $\sigma_h = 38$ MPa, $P_{inj} = 38$ MPa, $P_{pro} = 7$ MPa, $T_s = 350$ °K, Ti = 320 °K

$$T(r,t) = T_0 + (T_w - T_0)L^{-1}\left\{\frac{1}{s}\frac{K_0\left(r\sqrt{s/c_0}\right)}{K_1\left(r_w\sqrt{s/c_0}\right)}\right\} \tag{73}$$

where, $\tilde{g}$ is the Laplace transformation of g and

$$\xi = r\sqrt{\frac{s}{c}} \tag{74}$$

$$\beta = r_w\sqrt{\frac{s}{c}} \tag{75}$$

K_0 and K_1 are the first order modified Bessel function of the first and second kind. Laplace inversion is solved using the method presented by Stehfest (1970). The solution in time is achieved by following formula:

The Laplace transformation can be inverted using

$$f(r,t) \approx \frac{ln2}{t}\sum_{n=1}^{N} C_n \overset{\approx}{f}\left(r, n\frac{ln2}{t}\right) \tag{76}$$

where (ln) represents the natural logarithm and

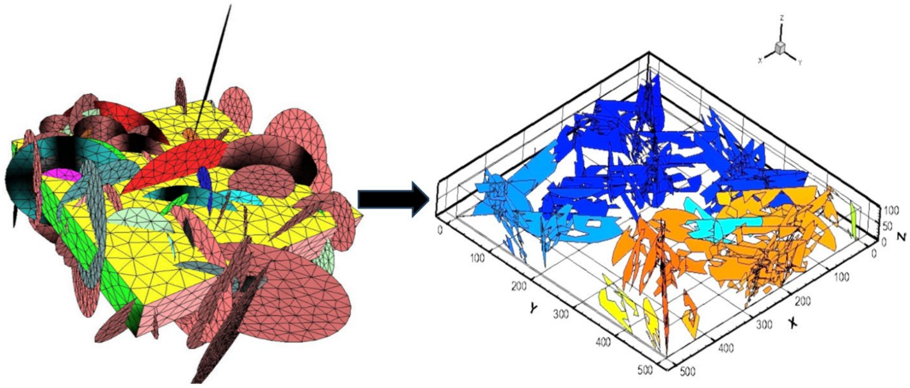

Fig. 6 Schematic representation of the discrete fracture network of the Soultz geothermal reservoir

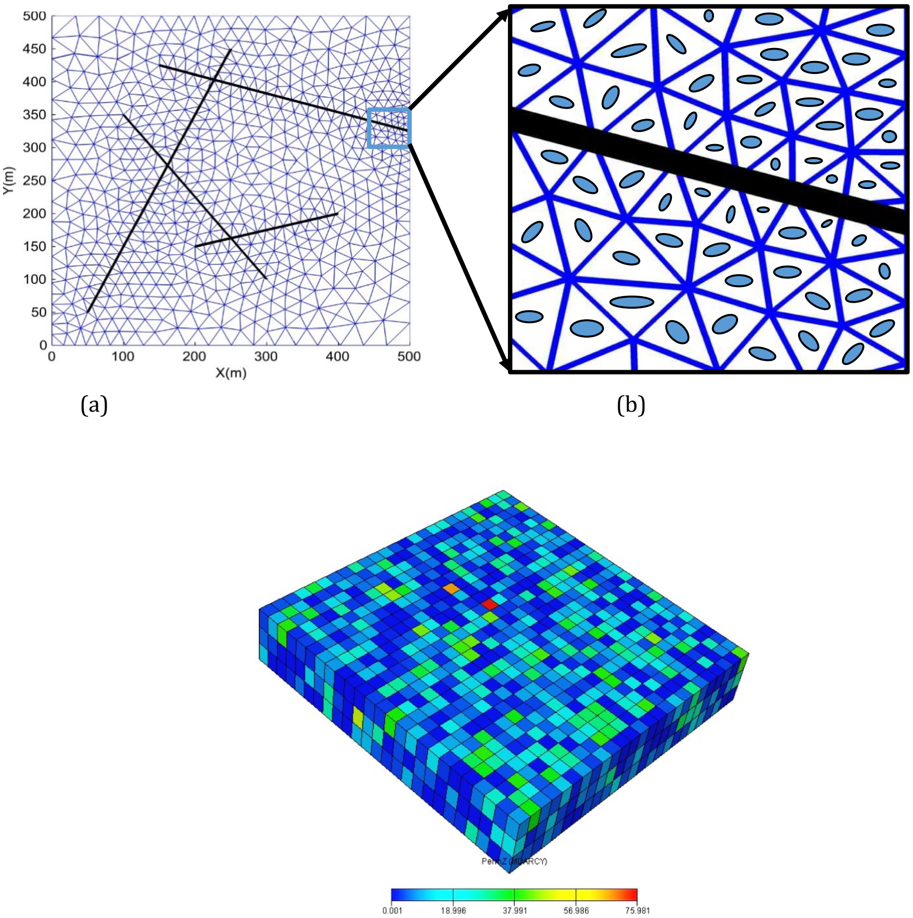

(a)

(b)

(c)

Fig. 7 **a** Discrete fracture network and **b** computed permeability tensor of the Soultz geothermal reservoir at a depth of 3650 m in 2D space and **c** computed permeability tensor of the Soultz geothermal reservoir in 3D space.

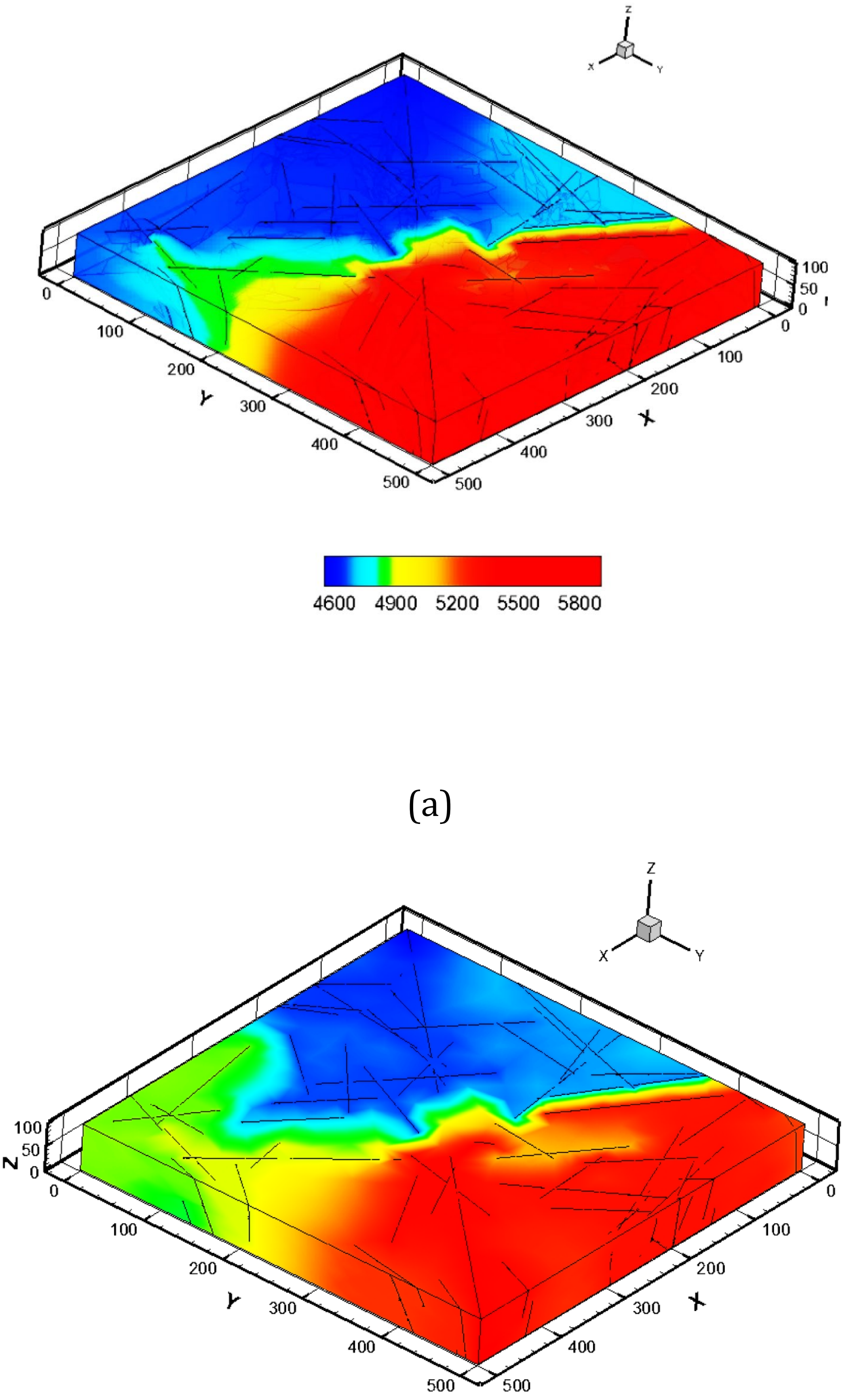

(a)

(b)

Fig. 8 Pore pressure distribution (top) after 2 years **a** and 7 years **b** of fluid injection for $\sigma_H = 55$ MPa (8000 psi), $\sigma_h = 57$ MPa (8276 psi), Pinj = 42 MPa (6100 psi), Pprod = 31.7 MPa (4700 psi), and Tinj = 80 °C

$$C_n = (-1)^{n+\frac{N}{2}} \sum_{k=(n+1)/2}^{min(n,N/2)} \frac{k^{N/2}(2k)!}{(N/2-k)!k!(k-1)!(n-k)!(2k-n)!} \tag{77}$$

The numerical results obtained were plotted against the analytical solutions in Figs. 4 and 5. The results present a good match between numerical and analytical solutions which endorses that the developed thermos-poro-elastic numerical model can be used in different field applications, (for more details about validation, see (Azim 2016).

Application of the in-house Simulator for real-field case study of Soultz geothermal

This study utilizes a novel methodology for creating a subsurface fracture map of the Soultz-Sous-Forets geothermal reservoir to understand the characteristics and fluid flow patterns of the reservoir (Baujard et al. 2021). By integrating various types of field data, including field and wellbore image data, the authors constructed a detailed representation of the reservoir fracture network (refer to Reda Abdel Azim (2021) for more details on the frame work used for development of reservoir fracture networks).

The depth of 3650 m for the fracture pattern indicates the extent of the fracture network within the geothermal reservoir. The presence of fractures at this depth suggests that the reservoir may extend to a significant depth, potentially increasing its heat reserves and longevity. The findings of this study on the long-term effects of cold fluid circulation on the Soultz-Sous-Forets geothermal reservoir are essential

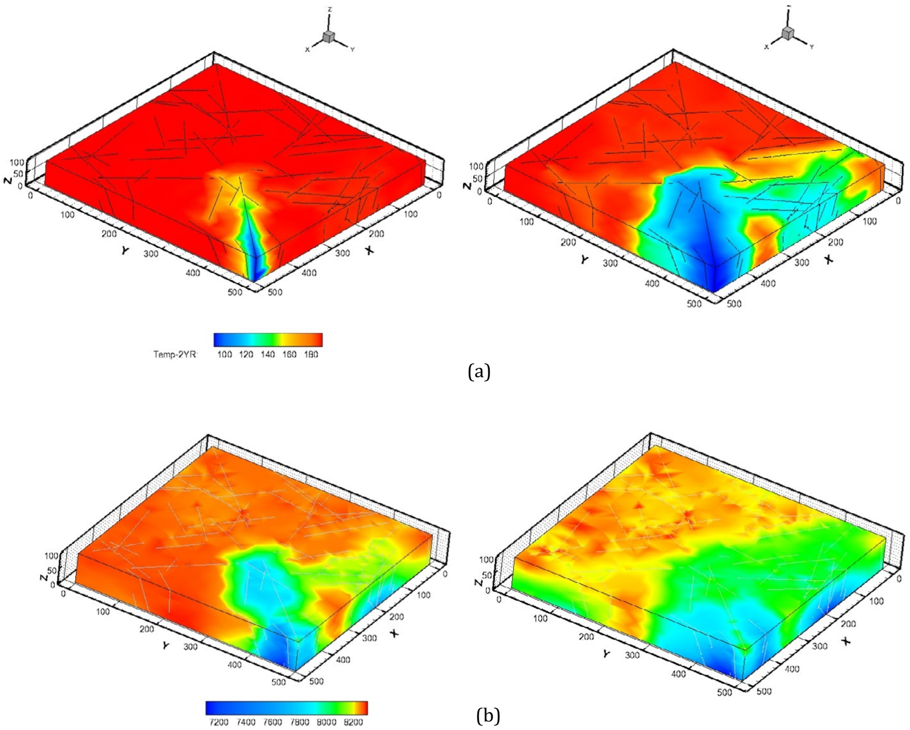

(a)

(b)

Fig. 9 Reservoir temperature drawdown (top) and thermal vertical stress (bottom) after **a** 2 years and **b** 7 years of production for $\sigma_H = 55$ MPa (8000 psi), $\sigma_h = 57$ MPa (8276 psi), Pinj = 42 MPa (6100 psi), Pprod = 31.7 MPa (4700 psi), and Tinj = 80 °C for optimizing its management and maximizing its energy production potential. By understanding the impact of cold fluid circulation on reservoir properties, such as temperature distribution, geothermal operators can design injection and production strategies that minimize adverse effects and enhance heat extraction.

Moreover, Fig. 6 shows the discretized mesh (triangular elements) of the domain. As stated in the earlier sections, the permeability tensors are calculated by considering short fractures (less than 40 m). Figure 7 shows how permeability tensors are computed for the Soultz reservoir. After the permeability tensors are computed, they are utilized to discretize long fractures (> 40 m) and simulate fluid flow and heat transfer to evaluate the reservoir's long-term response over a 14-year production period. The reservoir characteristics that are considered for this investigation are listed in Table 2.

Figure 8a, b clearly illustrates the evolution of fluid flow patterns within the Soultz geothermal reservoir over time. After two years of production, the pore pressure distribution indicates that the fluid primarily flows through a network of long, interconnected fractures. This suggests that the reservoir fracture network plays a dominant role in facilitating fluid movement during the initial production phase.

However, after 7 years of production, the injection pressure distribution shows a significant shift, with the pressure front advancing considerably closer to the producing well. This indicates that the fluid has spread more extensively throughout the reservoir and is no longer confined to the primary fracture network. This increase in fluid flow suggests that the reservoir's permeability has increased over time, allowing fluid to permeate through a broader area of the reservoir.

The observed changes in fluid flow patterns over time highlight the importance of considering the long-term effects of production on geothermal reservoirs. Understanding how fluid flow evolves over time is crucial for optimizing injection and production strategies to maximize heat extraction and extend a reservoir's lifespan.

The results presented in Fig. 9a, b provide valuable insights into the heat transfer dynamics within the Soultz geothermal reservoir during production. The observed temperature drop in the vicinity of the wellbore during the two years of production is consistent with the initial fluid flow patterns, where fluid circulation was primarily focused on the fracture network near the wells.

As production progressed over a 7-year period, the fluid movement occurred in an increasing portion of the reservoir, leading to more extensive heat exchange between the rock matrix and the fluid. This increased heat transfer is reflected in the broader temperature drop observed across the reservoir.

A comparison of these results with those from an earlier study by Koh et al. (2011) highlights the significance of considering local thermal nonequilibrium (LTNE) in modelling heat transfer processes. The LTNE approach, employed in the current study, accounts for the temperature differences between the rock matrix and the fluid, providing a more accurate representation of heat transfer in geothermal reservoirs.

The substantial decrease in the average matrix temperature from 200 to 180 °C after 7 years of production demonstrates the impact of fluid circulation on the reservoir's thermal state. This temperature drop is a crucial factor to consider when evaluating the long-term energy production potential of reservoirs and designing sustainable management strategies. In addition, the effective stresses (see Fig. 9a, b, bottom) can

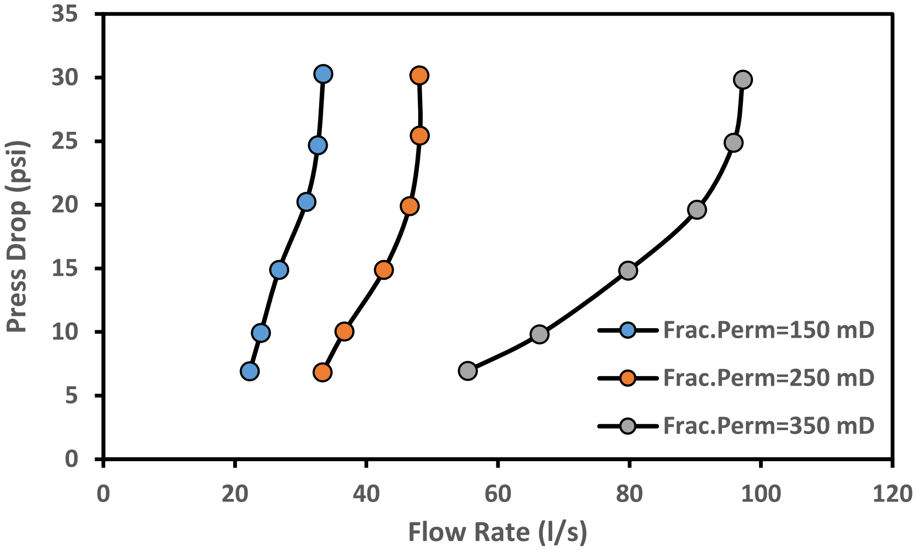

Fig. 10 Pressure loss as a function of flow rate at different fracture permeabilities

be significantly affected by cold water circulation after 2 and 7 years of cold-water injection due to the thermal stresses. The thermal stresses can also cause tensile stresses to develop in the rock matrix, which can lead to tensile fractures. The overall effect of cold-water circulation on the effective stresses in a fractured reservoir is that it increases the compressive stresses in the cooled zones and reduces the effective stresses in the surrounding rock matrix. Thermal stresses can play a significant role in this process, especially in the early stages of cold-water injection.

Three distinct average fracture permeability values (150, 250, and 350 mD) of the Soultz geothermal reservoir are considered to investigate the impact of the hot water flow rate on pressure loss between the injector and producers. Figure 10 presents the pressure loss as a function of different fracture permeability. The figure illustrates how the rate of hot water generation can be considerably increased for a given pressure loss by increasing the average fracture permeability. For instance, a hot water production rate of 20 l/s can be attained for an average fracture permeability of 150 mD, given a pressure loss of 7 MPa between an injector and a producer (separated at a distance of 700 m). For a given average fracture permeability of 350 mD, the production rate increases to 55 l/s.

The findings presented in Fig. 10 highlight the critical role of reservoir permeability in influencing fluid production rates and pressure drops in geothermal reservoirs. The results indicate that a higher average fracture permeability of 350 mD leads to a significant increase in hot water production, reaching up to 90 l/s, compared to an inadequate 30 l/s with an average fracture permeability of 150 mD.

This observation emphasizes the importance of accurately characterizing reservoir permeability to optimize production strategies and maximize energy extraction. A higher permeability facilitates more efficient fluid flow, reducing the pressure drop between injection and production wells and enabling higher production rates. This study also suggests that a commercial flow rate of 60–90 l/s can be achieved with an

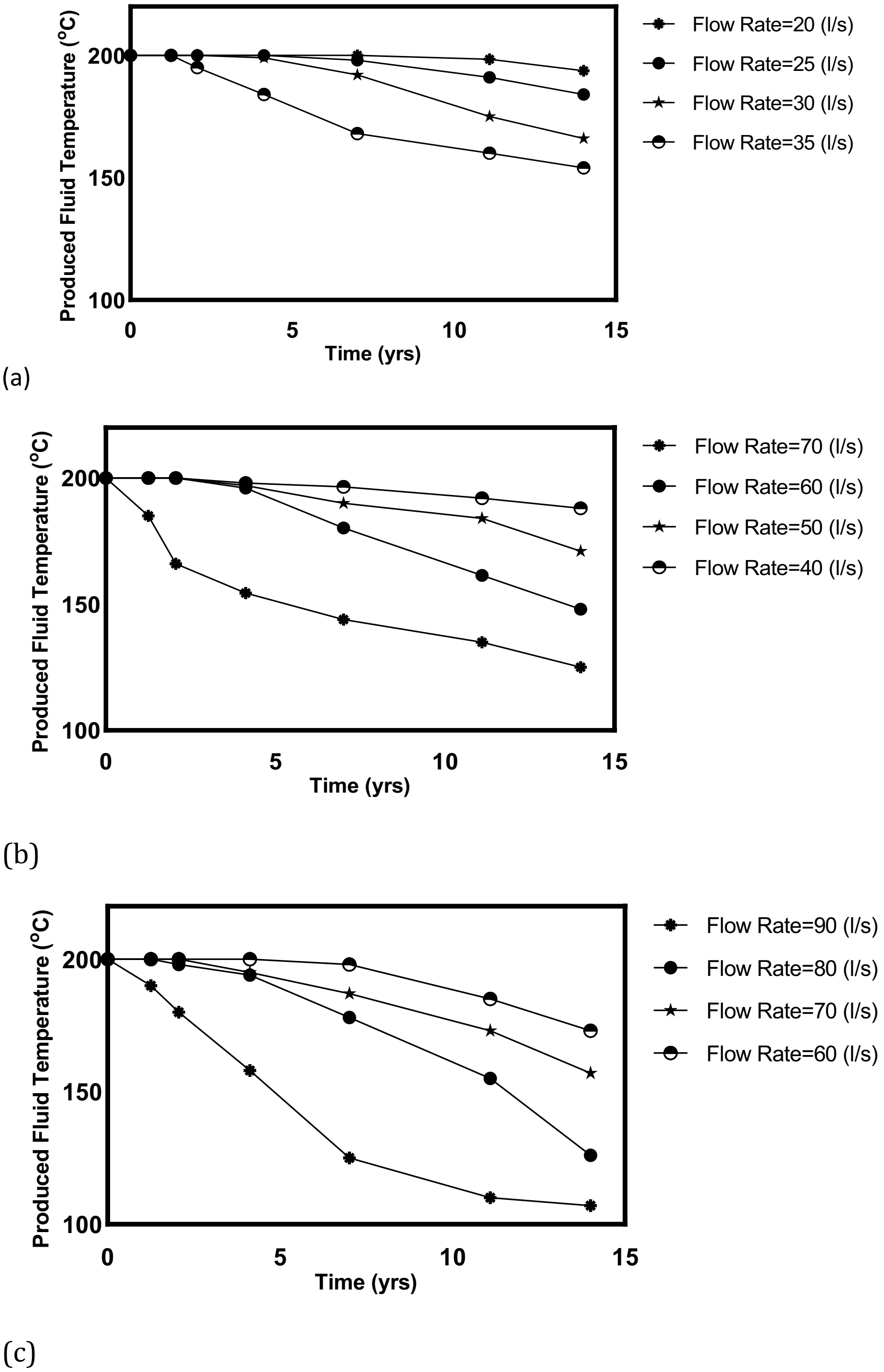

(a)

(b)

(c)

Fig. 11 Temperature of the produced fluid versus production time at different injection flow rates for **a** k = 150 md, **b** k = 250 md, and **c** k = 350 (md) with σ_H = 55 MPa (8000 psi), σ_h = 57 MPa (8276 psi), and Tinj = 80 °C

appropriate pressure loss of 14 MPa, provided that the average reservoir fracture permeability exceeds 150 mD. This information is valuable for geothermal operators when evaluating the potential of geothermal reservoirs and designing production plans.

The technical feasibility of achieving a 14 MPa pressure loss between injection and production wells depends on several factors, including the wellbore configuration, pumping capacity, and reservoir characteristics. Careful consideration of these factors is essential for designing efficient and cost-effective geothermal energy production systems.

Several numerical experiments are carried out to investigate the impact of the average fracture permeability and water flow rate on heat transfer from the matrix into the fluid and the resulting increase in the produced water temperature. Three average fracture permeabilities—150, 250, and 350 mD—are considered throughout this investigation. The flow rates are adjusted from 20 to 90 l/s. The reservoir temperature is initially maintained at 200 °C. For fifteen years, the temperature of the produced water is observed. The model's findings are displayed in Fig. 11 which present the temperature of the produced fluid versus production time at different combination of injection flow rates and average fracture permeability. Based on the provided information, it appears that the temperature of the water produced from fractured reservoirs exhibits a complex relationship with fracture permeability and flow rate. While the temperature remains relatively constant for the initial production period, it subsequently declines at varying rates depending on the specific permeability and flow rate conditions.

The observed behaviour suggests that the temperature of the produced water is influenced by the interplay between the heat transfer mechanisms and fluid flow characteristics within the fractured reservoir. A higher fracture permeability generally facilitates faster fluid flow, leading to a quicker decrease in the produced water temperature (see Fig. 11c). However, this trend is not always linear, as evidenced by the prolonged high temperature observed for low permeability and low flow rate conditions. This could be attributed to a reduced heat transfer due to slower fluid movement within the reservoir and thus a longer retention time.

Despite the potential benefits of high produced water temperatures for thermal applications, commercial viability of low-permeability reservoirs is hindered by low water production rates. On the other hand, high-permeability reservoirs offer the potential for high production rates at reasonable pressure losses, but the reservoir life is still relatively short, even if high produced water temperatures are maintained.

These findings highlight the importance of considering both fracture permeability and flow rate when evaluating the potential for thermal applications in fractured reservoirs. While a higher permeability generally leads to a greater production rate, it also contributes to a faster decline in the produced water temperature. Balancing these factors is crucial for optimizing thermal applications and achieving long-term economic viability.

In summary, the relationships among the produced water temperature, fracture permeability, and flow rate are intricate and require careful consideration when designing and implementing thermal applications in fractured reservoirs. A comprehensive understanding of these factors is essential for maximizing energy recovery and achieving sustainable resource utilization.

The results presented in Fig. 12 demonstrate a direct correlation between the production rate and recovery factor for fractured reservoirs with varying permeability values. As the production rate increases, the recovery factor also increases, reaching a plateau

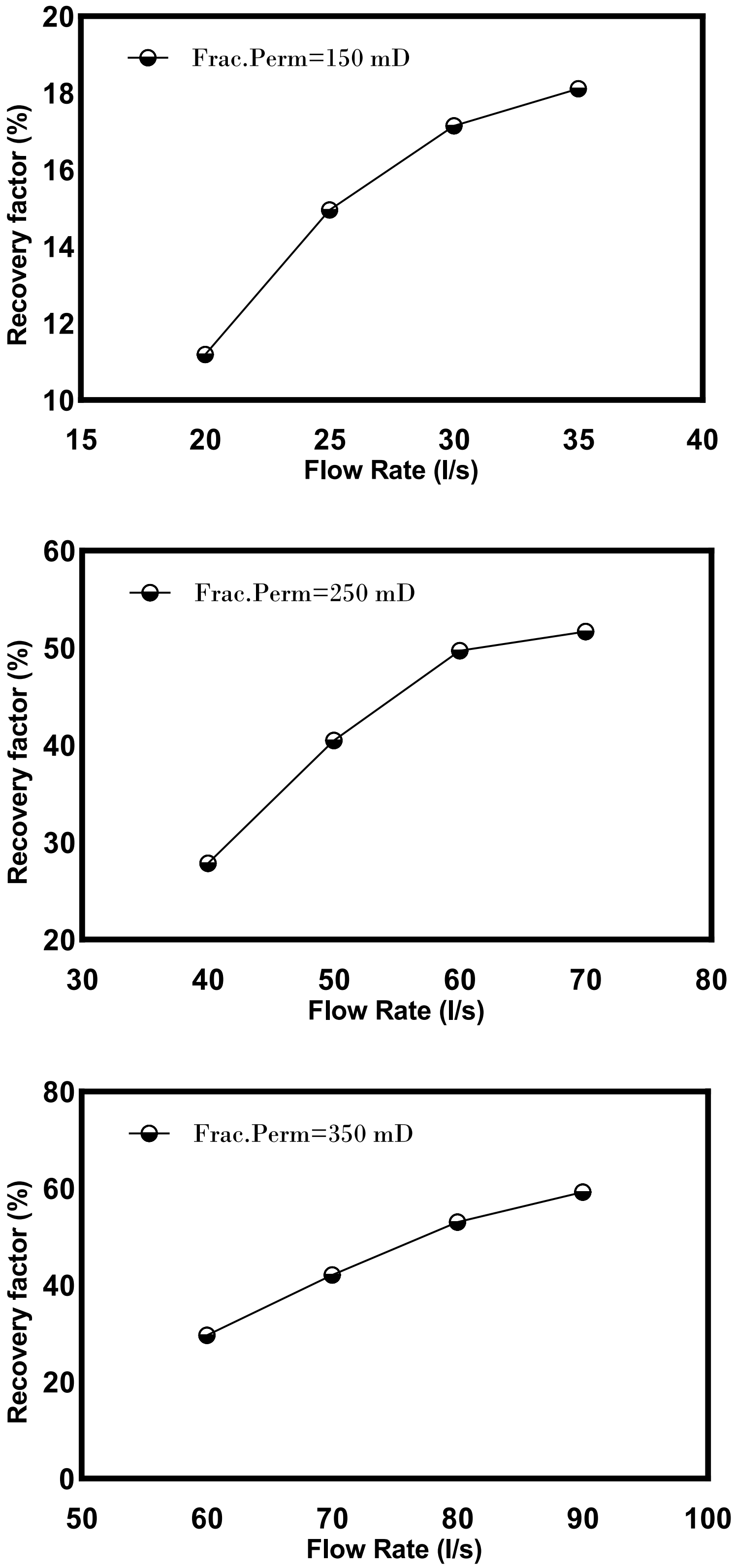

Fig. 12 Recovery factor versus flow rate at different fracture permeabilities: **a** k = 150 md, **b** k = 250 md, and **c** k = 350 md with $\sigma_H = 55$ MPa (8000 psi), $\sigma_h = 57$ MPa (8276 psi), and Tinj = 80 °C

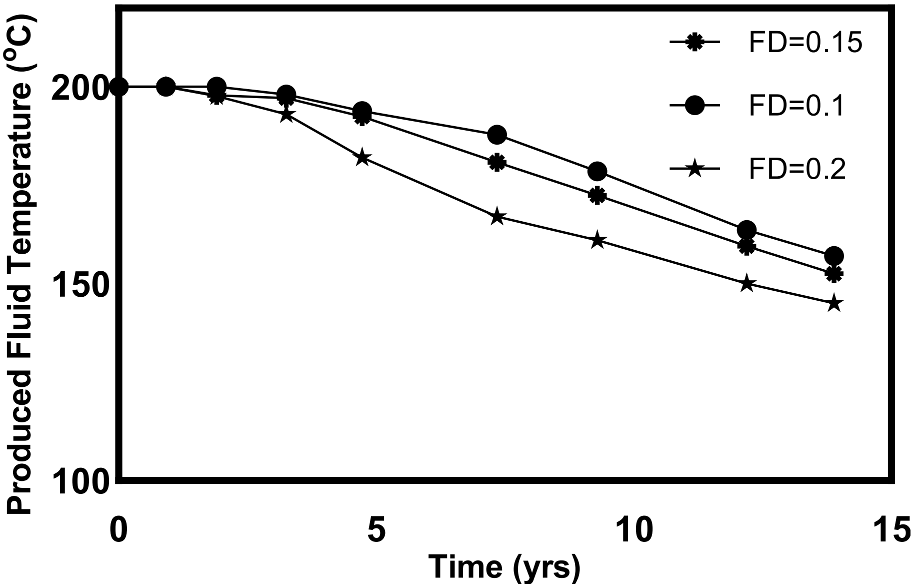

Fig. 13 Fluid temperature distribution for different FDs for $\sigma_H = 55$ MPa (8000 psi), $\sigma_h = 57$ MPa (8276 psi), and Tinj = 80 °C

at a specific flow rate. This optimal flow rate corresponds to the maximum achievable recovery factor for a given fracture permeability. The recovery factor is defined as the ratio of the actual extracted heat to the original heat reserve.

The observed behaviour can be attributed to the relationship between the fluid flow and heat transfer processes within the fractured reservoir. At lower production rates, the fluid has more time to interact with the rock matrix, enhancing heat transfer and facilitating energy extraction. However, as the flow rate increases, the fluid spends less time within the reservoir, limiting the extent of heat transfer.

The optimal flow rate for each fracture permeability condition represents the balance between maximizing fluid sweep through the fracture network and allowing sufficient time for heat transfer to occur. Exceeding this optimal flow rate does not further enhance heat extraction, as the fluid's residence time within the reservoir becomes too short.

The results align with observations from geothermal reservoirs, as noted by Sanyal and Butler (2005), and highlight the importance of optimizing production rates to achieve maximum energy recovery from fractured reservoirs. Thus, Careful consideration of fracture permeability and flow rate is crucial for designing and implementing effective thermal recovery strategies.

The observations presented in Fig. 13 highlight the influence of fracture density on the decrease in temperature of the produced fluid in geothermal reservoirs. For reservoirs with high fracture density (FD = 0.2), the produced fluid temperature remains relatively constant for the first two years of circulation, indicating efficient heat transfer from the rock matrix to the fluid. However, a rapid decrease in the produced fluid temperature is observed during the subsequent two years, suggesting a decrease in heat transfer efficiency due to the depletion of hotter fluid from the fracture network.

Reservoirs with lower fracture density exhibit a slower decline in the produced fluid temperature, with the maximum drawdown observed after four years of circulation. This slower temperature decrease is attributed to the reduced fracture network, which allows the reservoir matrix to retain higher temperatures for a longer period.

The findings from Fig. 13 emphasize the importance of considering fracture density when evaluating the long-term performance of geothermal reservoirs. Reservoirs with higher fracture density may initially produce hotter fluids, but their temperature declines more rapidly due to the depletion of hot fluid from the fracture network. Conversely, reservoirs with lower fracture density may initially produce cooler fluids, but their temperature decreases more slowly, allowing for longer periods of sustained heat extraction.

Effective geothermal reservoir management strategies should consider fracture density as a key factor in optimizing fluid production and heat extraction over a reservoir's lifetime. By understanding the interplay between fracture density, fluid flow, and heat transfer, geothermal operators can make informed decisions about well placement, production rates, and reservoir stimulation techniques to maximize energy recovery and extend the reservoir's productive life.

Conclusion

This study presents an integrated thermo-poro-elastic model based on the finite element technique to estimate the temperature of the generated fluid and simulate fluid flow in fractured geothermal reservoirs. In addition, a sensitivity study was carried out to investigate how different reservoir factors affect the temperature of the produced fluid. Based on the data, it was concluded that the reservoir fluid temperature drawdown is significantly impacted by the fracture aperture. In addition, to maintain a long-term sustainable reservoir fluid temperature during the circulation period, estimating the injection flow rate is crucial.

For a longer period, a high produced water temperature can be achieved with a low fracture permeability and high fluid retention time. Slower fluid movement minimizes frictional heat loss and allows more time for heat transfer from the rock, leading to initially higher temperatures as a result of low permeability. However, to achieve a commercial flow rate (60–90 l/s) at a reasonable pressure loss (equivalent to or below 14 MPa), the average reservoir fracture permeability must be greater than 100 mD. Increases in the fluid flow rate and fracture permeability were shown to cause a decrease in the matrix temperature, which in turn decreased the generated fluid temperature and increased the thermal recovery factor. The thermal recovery factor represents the percentage of the total reservoir heat extracted. Even with a slight decrease in the generated fluid temperature, the energy extraction rate can increase due to the higher flow rate, potentially leading to an increase in the thermal recovery factor. On the other hand, an ideal flow rate arises when the recovery factor is maximized.

Appendix A

See Figs. 14 and 15 here.

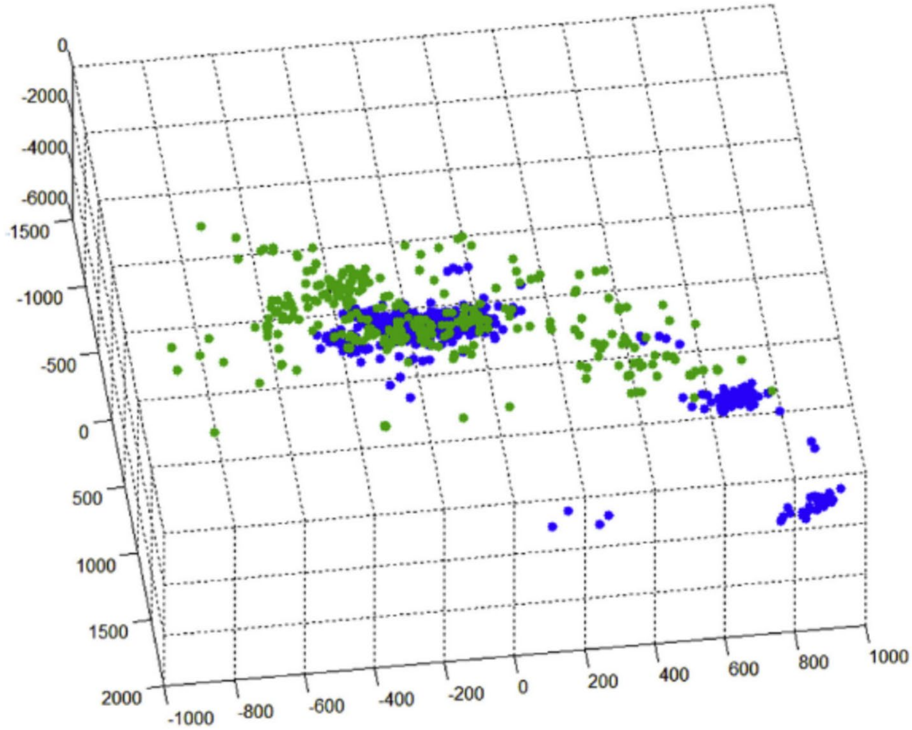

Fig. 14 Comparison between the simulated dilation events (green circles) with that from the field test trial (blue circles) with $\sigma_H = 44.8$ MPa, $\sigma_h = 41$ MPa, $\sigma_v = 49.64$ MPa, $P_{inj} = 55$ MPa and $P_i = 35.16$ MPa after 30 days of cold-water injection

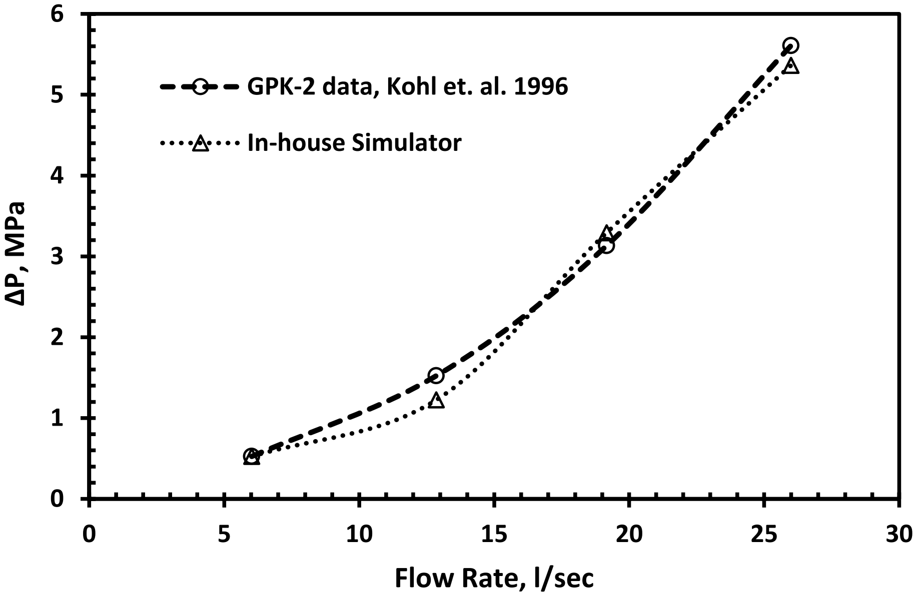

Fig. 15 Comparison between the simulated differential pressure and the real field data (injectivity-test) of Well GPK-2

The in-house simulator was verified by the first author in previous study against a field test of the Habanero geothermal reservoir located in Cooper Basin, South Australia

(Azim 2020). The field test of Habanero geothermal reservoir took place through injection of cold water into the reservoir for a period of 12 days to test reservoir response to cold water injection. That is, during this test period the the location and magnitude of shear dilation events (i.e., the changes in fracture aperture) were monitored. Then the in-house thermo-Poro elastic numerical model was used to calculate fracture aperture changes and locate the shear dilation events. A comparison of the location and magnitude of micro-seismic events (shear dilation events) formed during the field test of Habanero geothermal reservoir and the ones predicted by the in-house simulator are presented in Fig. 14. In this figure, the blue circles represent events generated from simulation process due to injection of fluid after 30 days and the green circles present the location of the dilation events from field observations. Results of this study show a close match between of them.

Moreover, further validation of the in-house simulator against operational history data of Soultz geothermal reservoir benefiting from existing publications of Kohl et al. (1995); Baria et al. 1999) is presented in this section.

Specifically, a history matching of operational history data (injectivity-test data) of Well GPK-2 in Soultz geothermal site (Kohl et al. 1995; Baria et al. 1999) was conducted using the in-house thermos-poro-elastic simulator. In this history matching process, the discrete fracture network map was generated by the statistical analysis of field data procedures developed by [59]. This technique integrates different field data to determine a distribution range of fracture properties (fracture orientation, fracture density, and fractal dimension). The determined fracture density and fractal dimension distributions are used as an input to an object based stochastic sequential Gaussian 3-D simulator to generate different random realization of fracture attributes, in this simulation the fractures are treated as circular disk objects as shown in Fig. 6 of the manuscript. Each fracture is defined based on its orientation (i.e.; the dip and azimuth angles of the fracture), center point (i.e., fracture location), radius and aperture. Moreover, random realization of fractures continue until the total fracture intensity and fractal dimension of the studied area are met, at this point the resulted model is the 3-D subsurface fracture map of the studied reservoir. Afterward, the generated 3-D subsurface map is divided into a number of grid blocks (N grid blocks) to calculate the grid-based permeability tensors as shown in Fig. 7A in the manuscript. For this purpose, a threshold fracture length (LF_{min}) is defined, accordingly fractures with a length less than the threshold fracture length that cut a certain block, are used to calculate the permeability tensors of that block (i.e.; fractures which have a length less than (LF_{min}) are considered as part of the matrix in the form of permeability tensor, in other word the short fractures are considered as a local spatial heterogeneity within the matrix block), as shown in Fig. 7B in the manuscript. Once the grid-based 3-D permeability tensors are calculated the matrix domain is coupled with the explicitly discretized long fractures (i.e.; fractures with fracture length $> LF_{min}$). The matrix domain is discretized by four-node tetrahedral elements while the triangular elements are used for discretization of explicit long fractures, as shown in Fig. 7C. The used grid blocks were built using an in-house developed mesh generator. Once the hybrid permeability tensor and discrete fracture mesh is ready then it is used in the in-house thermos-poro-elastic model to simulate the flow in the fractured geothermal reservoir and history match the injectivity-test data of Well GPK-2.

The history matching process can be summarized as follows:

1. Generate the subsurface fracture realization using field data procedures developed by Doonechaly and Rahman (2012).
2. Utilizing periodic boundary conditions (Durlofsky 1991), calculate the block-based permeability tensor of the single continuum taking into account the short fractures.
3. Couple the block-based permeability tensor with the discrete fracture network of long fractures using the in-house mesh generator (hybrid approach).
4. Start the in-house model to simulate cold water injection into the geothermal reservoir.
5. Compare the in-house simulator results with that of the measured production data if Well GPK-2 to estimate the error.
6. If the error from step 5 is less than the predefined error threshold then stops and report the optimum fracture realization with the production temperature results. Otherwise, go back to step 1 to modify fracture attribute and generate new fracture realization. The simulated well-production results are compared with that from field operational data for each realization until the error is minimized.

Accordingly, a comparison of Well GPK-2 injectivity-test data and the in-house simulator is presented in Fig. 15, it can be seen that the in-house simulator results of differential pressure versus flow rate is in good agreement with that of GPK-2 real field injectivity-test data.

Acknowledgements
The authors would like to acknowledge King Abdulaziz University for supporting this research.

Author contributions
Reda Abdel Azim: conceptualization, software, data curation, formal analysis, writing—original draft, writing—review and editing. Saad Alatefi: conceptualization, formal analysis, writing—review and editing. Abdulrahman Aljehani: formal analysis, data curation.

Funding
This research work was funded by Institutional Fund Projects under grant no. (IFPIP: 440-145- 1443).

Availability of data and materials
The data sets used or analysed during the current study are available from the corresponding author upon reasonable request.

Declarations

Competing interests
No conflicts of interest exist in the submission of this manuscript, and the manuscript has been approved by all the authors for publication. The manuscript has not been previously published, is not currently submitted for review to any other journal, and will not be submitted elsewhere before a decision is made by this journal.

Received: 23 November 2023 Accepted: 2 July 2024

References

Abdel Azim R, Alatefi S, Alkouh A. A coupled poro-elastic fluid flow simulator for naturally fractured reservoirs. Energies. 2023;16:6476.

Andre L, Rabemanana V, Vuataz FOD. Influence of water? Rock interactions on fracture permeability of the deep reservoir at Soultz-sous-Forets. France Geother. 2006;35:507–31.

Azim RA. Integration of static and dynamic reservoir data to optimize the generation of subsurface fracture map. J Petrol Explor Product Technol. 2016;6:691–703.

Azim RA. A hybrid simulation approach to evaluate stimulation micro-seismic events and production potential of fractured geothermal reservoirs. Petrol Res. 2020;5(2):131–43.

Azim RA. Estimation of fracture network properties from FMI and conventional well logs data using artificial neural network. Upstream Oil Gas Technol. 2021;7:100044.

Baria R, Baumgartner J, Gerard A, Jung R, Garnish J. European HDR research programme at Soultz-sous-Forets (France) 1987–1996. Geothermics. 1999;28:655–69.

Bathe K-J. Finite element procedures. Upper Saddle River: Prentice Hall; 1996.

Baujard C, Rolin P, Dalmais É, Hehn R, Genter A. Soultz-sous-Forêts geothermal reservoir: structural model update and thermo-hydraulic numerical simulations based on three years of operation data. Geosciences. 2021;11(12):502.

Berre I, Doster F, Keilegavlen E. Flow in fractured porous media: a review of conceptual models and discretization approaches. Transp Porous Media. 2019;130(1):215–36.

Bolton EW, Lasaga AC, Rye DM. A model for the kinetic control of quartz dissolution and precipitation in porous media flow with spatially variable permeability: formulation and examples of thermal convection. J Geophys Res. 1996;101(B10):22157–87.

Bourbiaux B. Fractured reservoir simulation: a challenging and rewarding issue. Oil Gas Sci Technol Revue De L'institut Français Du Pétrole. 2010;65(2):227–38.

Breede K, Dzebisashvili K, Liu X, Falcone G. A systematic review of enhanced (or engineered) geothermal systems: past, present and future. Geotherm Energy. 2013;1:1–27.

Demirel, Y. Heat Storage by Phase Changing Materials and Thermo-economics. in: paksoy, h.ö. (eds) thermal energy storage for sustainable energy consumption. nato science series, 2007vol 234. springer. https://doi.org/10.1007/978-1-4020-5290-3_7

Doonechaly NG, Rahman S. 3D hybrid tectono-stochastic modeling of naturally fractured reservoir: application of finite element method and stochastic simulation technique. Tectonophysics. 2012;541:43–56.

Durlofsky LJ. Numerical calculation of equivalent grid block permeability tensors for heterogeneous porous media. Water Res Res. 1991;27(5):699–708.

Gholizadeh Doonechaly N, Abdel Azim R, Rahman SS. Evaluation of recoverable energy potential from enhanced geothermal systems: a sensitivity analysis in a poro-thermo-elastic framework. Geofluids. 2016;16(3):384–95.

Gong F, Guo T, Sun W, Li Z, Yang B, Chen Y, Qu Z. Evaluation of geothermal energy extraction in enhanced geothermal system (EGS) with multiple fracturing horizontal wells (MFHW). Renew Energy. 2020;151:1339–51.

Gupta A, Penuela G, Avila R. An integrated approach to the determination of permeability tensors for naturally fractured reservoirs. J Can Petrol Technol. 2001. https://doi.org/10.2118/01-12-02.

Hussain ST, Rahman SS, Azim RA, Haryono D, Regenauer-Lieb K. Multiphase fluid flow through fractured porous media supported by innovative laboratory and numerical methods for estimating relative permeability. Energy Fuels. 2021;35(21):17372–88.

Kazemi H. Pressure transient analysis of naturally fractured reservoirs with uniform fracture distribution, SPEJ 1969 451; Trans., AIME, 246.

Kazemi H, Merrill L Jr, Porterfield K. Zeman P Numerical simulation of water–oil flow in naturally fractured reservoirs. Soc Petrol Eng J. 1976;16(06):317–26.

Kelkar S, WoldeGabriel G, Rehfeldt K. Lessons learned from the pioneering hot dry rock project at Fenton Hill. USA Geotherm. 2016;63:5–14.

Khoei AR, Mortazavi SMS. Thermo-hydro-mechanical modeling of fracturing porous media with two-phase fluid flow using X-FEM technique. Int J Numer Anal Methods Geomech. 2020;44(18):2430–72.

Kim J-G, Deo MD. Finite element, discrete-fracture model for multiphase flow in porous media. AIChE J. 2000. https://doi.org/10.1002/aic.690460604.

Kirsch G. Theory of elasticity and application in strength of materials. Z Ver Dtsch Ing. 1898;42(29):797–807.

Koh J, Roshan H, Rahman SS. A numerical study on the long term thermo-poroelastic effects of cold-water injection into naturally fractured geothermal reservoirs. Comput Geotech. 2011;38:669–82.

Kohl T, Jung R, Hopkirk R, Rybach L. Non-linear flow transients in fractured rock masses-the 1995 injection experiment in Soultz. Proceedings of the 21st Workshop for Geothermal Reservoir Engineering, 1996.

Li T, Han D, Yang F, Li J, Wang D, Yu B, Wei J. Modeling study of the thermal-hydraulic-mechanical coupling process for EGS based on the framework of EDFM and XFEM. Geothermics. 2021;89:101953.

Mortazavi SMS, Rezaie Beydokhti O, Khoei AR. Modeling enhanced geothermal systems using a hybrid XFEM–ECM technique. Appl Therm Eng. 2023;230:120755.

Noorishad J, Mehran M. An upstream finite element method for solution of transient transport equation in fractured porous media. Water Resour Res. 1982;18(3):588.

Olasolo P, Juárez MC, Morales MP, Damico S, Liarte IA. Enhanced geothermal systems (EGS): a review. Renew Sustain Energy Rev. 2016;56:133–44.

Park YC and Sung WM. Development of FEM reservoir model equipped with effective permeability tensor and its application to naturally fractured reservoirs. In *SPE* International Oil and Gas Conference and Exhibition in China*,* 2000; 10: 10–18.

Quandalle P, Sabathier J. Typical features of a multipurpose reservoir simulator. SPE Reserv Eng. 1989;4(04):475–80.

Ramirez B, Kazemi H, Al-kobaisi M, Ozkan E, Atan S. A critical review for proper use of water/oil/gas transfer functions in dual-porosity naturally fractured reservoirs: part I. SPE Reserv Eval Eng. 2009;12(02):200–10.

Salimzadeh S, Paluszny A, Nick HM, Zimmerman RW. A three-dimensional coupled thermo-hydro-mechanical model for deformable fractured geothermal systems. Geothermics. 2018;71:212–24.

Sanyal SK, Butler SJ. An analysis of power generation prospects from enhanced geothermal systems. Geotherm Res Council Trans. 2005;29:131–8.

Snow DT. Anisotropie permeability of fractured media. Water Resour Res. 1969;5(6):1273–89.

Soltani M, Moradi Kashkooli F, Dehghani-Sanij AR, Nokhosteen A, Ahmadi Joughi A, Gharali K, Mahbaz SB, Dusseault MB. A comprehensive review of geothermal energy evolution and development. Int J Green Energy. 2019;16(13):971–1009.

Steefel CI, Lichtner PC. Multicomponent reactive transport in discrete fractures: controls on reaction front geometry. J Hydrol. 1998;209(1–4):186–99.

Stehfest H. Algorithm 368: numerical inversion of laplace transform. Commun ACM. 1970;13:47–9.

Sudicky EA, Frind EO. Contaminant transport in fractured porous media: analytical solutions for a system of parallel fractures. Water Resour Res. 1982;18(6):1634–42.
Sudicky E, McLaren R. The Laplace transform Galerkin technique for large-scale simulation of mass transport in discretely fractured porous formations. Water Resour Res. 1992;28(2):499–514.
Sun ZZ, Zhang X, Xu Y, Yao J, Wang H, Lv S, Sun ZZ, Huang Y, Cai M, Huang X. Numerical simulation of the heat extraction in EGS with thermal-hydraulic-mechanical coupling method based on discrete fractures model. Energy. 2017;120:20–33.
Teimoori A, Chen Z, Rahman SS, Tran T. Effective permeability calculation using boundary element method in naturally fractured reservoirs pages. Petrol Sci Technol. 2004;23:693–709.
Tenzer H, Park C-H, Kolditz O, McDermott CI. Application of the geomechanical facies approach and comparison of exploration and evaluation methods used at Soultz-sous-Forets (France) and Spa Urach (Germany) geothermal sites. EnviroN Earth Sci. 2010;61:853–80.
Thomas LK, Dixon TN, Pierson RG. Fractured reservoir simulation. SPEJ. 1983. https://doi.org/10.2118/9305-PA.
Turcotte D, Schubert G. Applications of continuum physics to geological problems. Hoboken: John Wiley & Sons; 1982.
Varnosfaderani AM, Gatmiri B, Haghighi EM. A model for moisture and heat flow in fractured unsaturated porous media Int. J Numer Anal Methods Geomech. 2017;41(6):828–58.
Watanabe N, Wang W, McDermott CI, Taniguchi T, Kolditz O. Uncertainty analysis of thermo-hydro-mechanical coupled processes in heterogeneous porous media. Comput Mech. 2010a;45:263–80.
Watanabe N, Wang W, McDermott C, Taniguchi T, Kolditz O. Uncertainty analysis of thermo–hydro–mechanical coupled processes in heterogeneous porous media. Comput Mech. 2010b;45:263–80.
Wei X, Feng Z, Zhao Y. Numerical simulation of thermo-hydro-mechanical coupling effect in mining fault-mode hot dry rock geothermal energy. Renew Energy. 2019;139:120–35.
Wu X, Yu L, Hassan NMS, Ma W, Liu G. Evaluation and optimization of heat extraction in enhanced geothermal system via failure area percentage renew. Energy. 2021;169:204-220L.
Zhang J, Xie J. Effect of reservoir's permeability and porosity on the performance of cellular development model for enhanced geothermal system. Renew Energy. 2020a;148:824–38.
Zhang J, Xie J. Effect of reservoir's permeability and porosity on the performance of cellular development model for enhanced geothermal system renew. Energy. 2020b;148:824–38.
Zhao Y, Feng Z, Feng Z, Yang D, Liang W. THM (Thermo-hydro-mechanical) coupled mathematical model of fractured media and numerical simulation of a 3D enhanced geothermal system at 573 K and buried depth 6000–7000 M. Energy. 2015;82:193–205.
Zhou L, Zhu Z, Xie X, Hu Y. Coupled thermal–hydraulic–mechanical model for an enhanced geothermal system and numerical analysis of its heat mining performance. Renew Energy. 2022;181:1440–58.
Zienkiewicz OC, Taylor RL. The finite element method: solid mechanics. Butterworth-Heinemann. 2000;2(5):155–74.

Publisher's Note